Contents

Part I

Introduction and Theoretical background

Chapter 1

Introduction

1.1 Double Beta Decay

Strong interest has been recently revived in neutrinoless double beta decay (DBD) by the discovery of neutrino oscillations in solar [1, 2], atmospheric [3], and reactor [4] experiments. This discovery indicates a non-zero value for the difference between two neutrino mass eigenvalues.

It becomes therefore imperative to search for a finite value for the effective electron neutrino mass [5, 6, 7]. In astrophysics, the recent results of the full sky microwave maps by WMAP together with the 2dF galaxy redshift survey [8] constrain to less than 0.7 eV the sum of the masses of neutrinos of the three flavors. Direct experiments on single beta decay presently constrain the absolute value of this mass to less than 2.2 eV, while a bound of 0.2 eV is expected in the KATRIN experiment [9].

A more restrictive limit for the effective mass of Majorana neutrinos can undoubtly come from neutrinoless double beta decay (DBD). In its two negatron channel DBD consists of the direct emission of two electrons from a nucleus (A,Z) decaying to the corresponding isobar (A,Z+2).

This rare nuclear transition was first proposed by Maria Goeppert-Mayer in 1935, and can be observed in nuclei for which the single beta transition from (A,Z) to (A,Z+1) is either energetically forbidden, or at least strongly

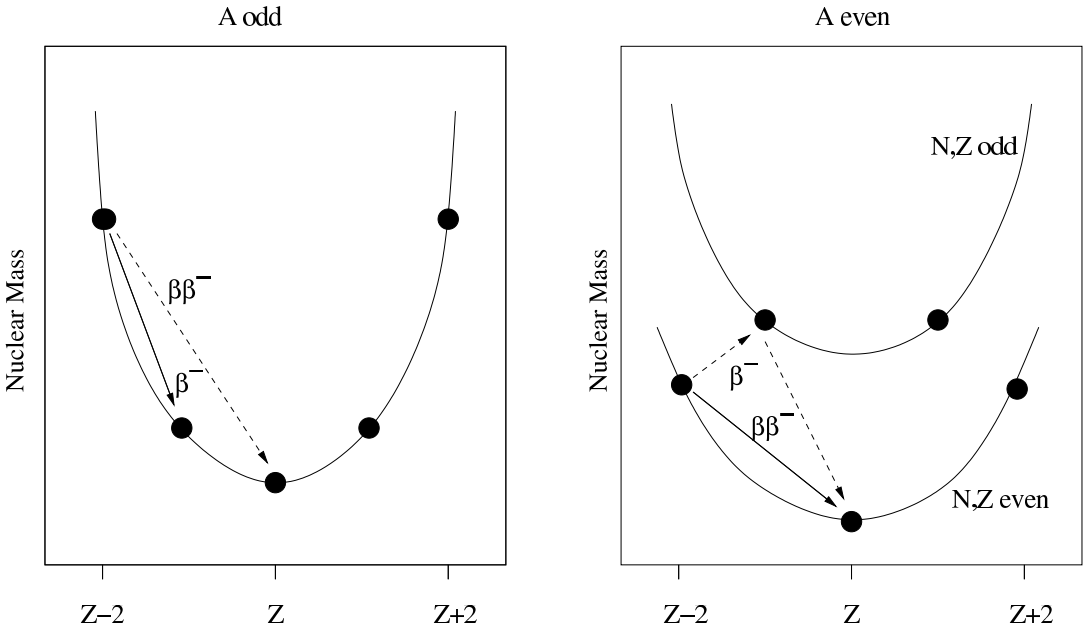

Figure 1.1: Two cases in which the double beta decay is energetically favoured. The binding energy of a nucleus increases when protons and neutrons are coupled to give a zero angular momentum. In the case in which the mass number, A, is even, the intermediate nucleus (A,Z+1) can have a binding energy smaller than that of the (A,Z+2) nucleus.

hindered by a large change of the spin-parity state, Figure (1.1).

The process of two neutrino DBD is accompanied by the emission of two electron anti-neutrinos and therefore conserves lepton number.

$$(A, Z) \rightarrow (A, Z + 2) + 2e + 2\bar{\nu_e}$$

It is allowed by the standard model of electroweak interactions, and it has been found in ten nuclei [10, 11, 12]. On the contrary conservation of the lepton number is violated in the majoron decay, where the massless Goldstone boson accompanies the emission of the two electrons, and in the so called neutrinoless DBD, where only the two electrons are emitted:

$$(A, Z) \rightarrow (A, Z + 2) + 2e$$

In this case these two particles would share the total transition energy and a peak would appear in the sum energy spectrum of the two electrons. In addition the available phase space is much larger with respect to the two neutrino one, rendering neutrinoless DBD a very powerful way to search for lepton number non-conservation.

The expected value for the effective neutrino mass, $\langle m \rangle$, or its upper limit is proportional to the square root of the rate, which makes searches for neutrinoless DBD quite difficult. On the other hand this rate is proportional to the square of the nuclear matrix element, whose evaluation is at least presently, quite uncertain. Since the uncertainty in the value of the nuclear matrix element reflects itself directly in that of $\langle m \rangle$, searches for neutrinoless DBD should be carried out on several candidate nuclei.

There is another reason for this statement; should a peak appear at the expected region of neutrinoless DBD, one cannot exclude a priori that it could be due to a line from a so far unknown radioactive contamination. Only the evidence for peaks at the different energy expected for a different DBD candidate nucleus would definitely prove the existence of neutrinoless double beta decay.

No evidence was claimed so far for the neutrinoless channel in any nucleus, with the exception of an alleged evidence for neutrinoless DBD of ^{76}Ge reported by a subset of the Heidelberg-Moscow Collaboration [13, 14], but confronted by other authors [5, 15, 16], and even by a different subset of the same collaboration [17].

1.1.1 Techniques for DBD search

The search for DBD can be performed with indirect measurements or with a direct measure.

- Indirect experiments are based on the search for the (A,Z+2) product nuclei, in radiochemical [18] or geochemical experiments [19, 20, 21, 22].

These experiments are very sensitive, but indicate only the presence of the daughter nucleus and cannot therefore discriminate between lepton conserving and non-conserving processes or between decays to the ground or excited states of the daughter nucleus.

- Direct experiments are based on two different approaches:
  - the detector itself is made of a material containing the double beta active nucleus: "calorimetric" experiments [23].
  - detector and sources are separated, and hence double beta active material must be inserted in the detector.

The use of cryogenic detectors to search for DBD was suggested in 1984 [24]. Bolometers are among the cryogenic detectors and are low temperature calorimeter. A single bolometer consists of three main systems: the *absorber*: in which the particle to be detected deposit its energy, resulting in a warming up of the absorber itself; the *sensor*, that is sensitive to thermal variations of the absorber; a *thermal sink* to which the absorber is weakly coupled.

An event, of energy ΔE, in the absorber heats it up and the temperature increase, ΔT, is in principle easily found, when the heat capacity, C of the absorber is known:

$$\Delta T = \frac{\Delta E}{C}$$

The absorbers are made with diamagnetic and dielectric crystals [25, 26], and therefore, at low temperature, their heat capacity is proportional to the cube of the ratio between the operating and Debye temperatures. As a consequence, in a cryogenic set-up the heat capacity of the absorber can become so small that even the tiny energy released by a particle in the form of heat generates a measurable temperature increase of the absorber.

Cryogenic detectors offer a wide choice of DBD candidates, the only requirement being that the candidate nucleus be part of a compound which can be grown in the form of a crystal with reasonable thermal and mechanical properties.

1.2 Cryogenic Underground Observatory for Rare Events

The proposed Cryogenic Underground Observatory for Rare Events (CUORE) experiment, and the forerunner Cuoricino, are experiments that aim to find a neutrinoless double beta decay. They are calorimetric experiments, hence direct experiments, in which the source of the searched decay is in the detector itself: ^{130}Te.

As a matter of fact, the isotope ^{130}Te is an excellent candidate to search for double beta decaydue to its high transition energy (2528.8±1.3 keV) [27], and large isotopic abundance (33.8%) which allows a sensitive experiment to be performed with natural tellurium. In addition, the expected signal at 2528.8 keV happens to be in an energy region between the peak and the Compton edge of the ^{208}Tl -rays at 2615 keV, which generally dominates the background in this high energy region.

Of the various compounds tellurium can make, TeO_2 appears to be the most promising one: it can be grown with good mechanical and thermal properties in large crystals of the order of a cube of 6 cm side.

A series of experiments with various arrays of 340 gram crystals of natural TeO_2 have been carried out in the Laboratori Nazionali del Gran Sasso. The results of an experiment carried out with an array of 16 crystals of natural Te and four enriched crystals of which two in ^{128}Te and two in ^{130}Te, with a total mass of $\approx$ 6.8 kg has been recently published [28].

1.2.1 Cuoricino

The Cuoricino array consists of a tower with 13 planes containing 62 crystals of TeO_2 operating in Hall A of the Gran Sasso Underground Laboratory [29] in the same dilution refrigerator previously used in our experiment with 20 crystals [28].

As shown in Figure (1.2), the structure is as follows: the upper 10 planes and the lowest one consist of 4 natural crystals of 5x5x5 cm^3, while the 11th

and 12th planes have nine, 3x3x6 cm^3 crystals. In the 3x3x6 cm^3 planes the central crystal is fully surrounded by the nearest neighbors.

The small size crystals are also made with natural tellurium except for four. Two of them are enriched in ^{128}Te and two in ^{130}Te, with isotopic abundance of 82.3 and 75%, respectively.

All crystals were grown with pre-tested low radioactivity material by the Shanghai Institute of Ceramics and shipped to Italy by sea in order to minimize the activation due to cosmic rays. They have then been lapped with specially selected low contamination abrasives to reduce the radioactive contamination on surface, introduced by the original production process in China. All these operations and the final mounting of the tower were carried out in a nitrogen atmosphere glove box in a clean room.

The mechanical structure of the array was made exclusively with OFHC Copper and Teflon, also previously tested for absence of measurable radioactive contaminations.

1.2.2 Bolometer

In the following we will describe the thermal model of the Cuoricino (CUORE) bolometer, Figure (1.3).

1. The bolometer of Cuoricino is made by an energy absorber of crystalline TeO_2, with a mass of 760 g and dimensions of 5x5x5 cm^3. The absorber contains the source of the searched double beta decay: about 10^{24} ^{130}Te nuclei.

2. The temperature variations of the absorber are measured by a Neutron Transmutation Doped Germanium thermistor. NTD Germanium is crystalline and hence its specific heat is reasonably low [30] and has a very steep dependence of the resistance with respect to the temperature (§(4.2)), and it is therefore a perfect candidate to make a sensitive thermometer for a bolometer. The NTD chip is used glued on the absorber by means of araldite.

Figure 1.2: The tower of CUORICINO and the four and nine crystal modules.

3. The weak links to the copper structure (thermal bath) are provided by the PTFE (or Teflon) parts that support the absorbers, but mainly by the boundary Kapitza resistance [31]. The PTFE supports have also a heat capacity.

4. Electrical connections to the thermometers are made by means of 50 μm diameter gold wires, that provide a direct thermal link of the thermometer to the heat sink.

The knowledge of all the parameters of the thermal model, Figure (1.3) is fundamental in the research and development, in order to improve the design of the bolometer but also in the interpretation of the acquired data.

During this work of thesis, we have carried out measurements on various kinds of thermal sensors of the detector both with the aim to enhance the knowledge of the parameters of the sensor, such as temperature dependence, §(4.2), or electron-phonon decoupling parameters, chapter 5, and to help in the design and production of the thermistor to better fit the needs of the bolometer.

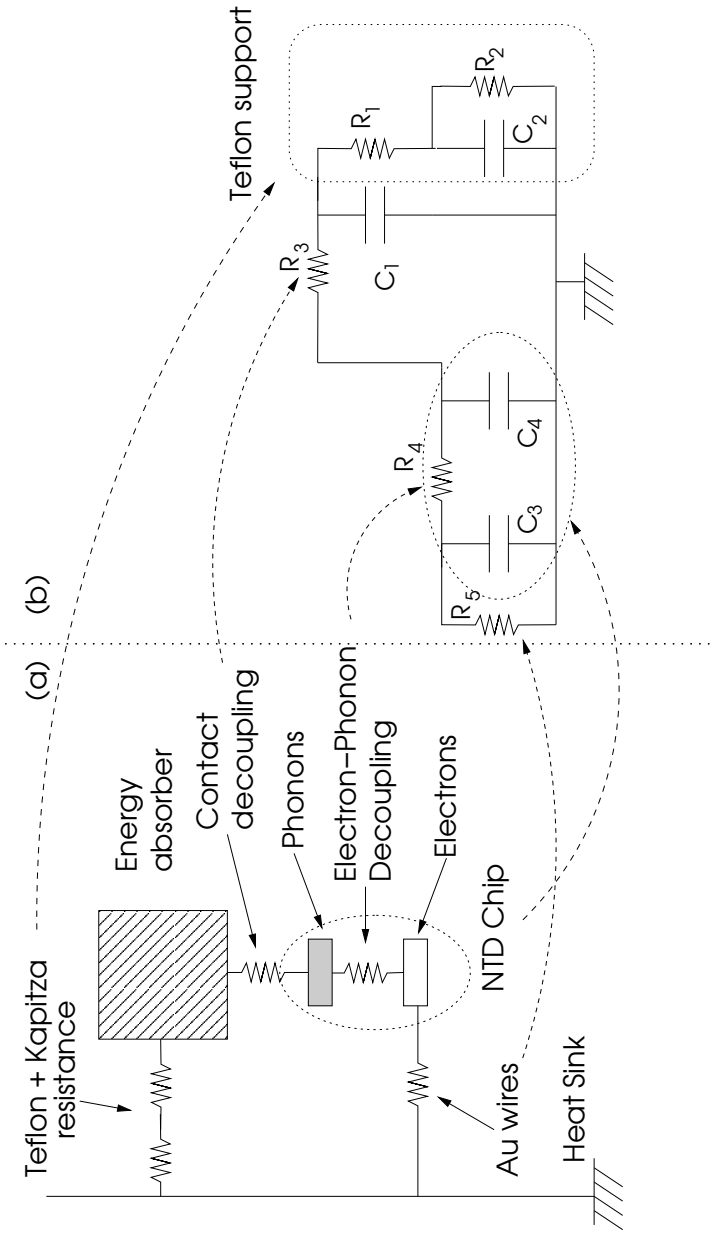

Figure 1.3: We show in part (a) the simplified thermal model of the bolometer. On the part (b) the equivalent electrical model is sketched. R_1 is the Kapitza resistance of the absorber-PTFE boundary; R_2 is the sum of the PTFE thermal resistance and of the PTFE-heat sink boundary; R_3 is the absorber-NTD boundary resistance; R_4 is the electron-phonon decoupling ; R_5 is the thermal resistance of the wires. C_1 is the absorber heat capacity, C_2 is the PTFE heat capacity, C_3 is NTD phonons heat capacity, C_4 is NTD electrons heat capacity.

Chapter 2

Theoretical Background

In this chapter we will present a brief summary of the theoretical background that involves the physics of doped semiconductors at low temperatures.

The theory is well settled and accounts for most of the transport characteristics of doped semiconductors systems. The main steps for the comprehension of their behaviour are: the Anderson localization, and the Mott's law, that we will see in §(2.1.2).

Anyway, some characteristics remain not explained by means of this theories, namely the ultra low temperature ($T < 40$ mK) strong non linearities in the Voltage Current curves (load curves) of NTD samples. Such non linearities are taken into account and explained by means of an empirical model described in §(2.2)

Finally in §(2.3) we will describe the theory of the influence of the magnetic field on such semiconductors.

2.1 Transport properties

2.1.1 Anderson localizations

We can use a tight binding method to calculate the band structure of conduction electrons in elements where electrons are strongly bound to the lattice

site. The wave function of such an electron (or charge carrier), is defined in the whole lattice but has a probability peak on a reticular site. The probability density of such an electron will be non negligible only on the nearest neighbourgs. This method can be applied to Si and Ge, since they have a not full d level. The charge carrier motion in such a system takes place by hopping from bound state to bound state.

We will see in §(4.1) that the process of doping modifies the semiconductor lattice, introducing elements usually different from the semiconductor atoms; generally the dopant atoms have one or two valence electrons more or less than the semiconductor atoms.

Since the doping process is a stocastic process, the lattice will host randomly distributed doping elements. In this way, the atomic energy level changes randomly from site to site.

Keeping in mind that the electrons are tight-bound to the lattice site, we can write the hamiltonian of an electron as a sum of a purely atomic part, and of a potential that enables the electron to hop from a bound state j to another bound state k:

$$\hat{H} = \hat{H}_0 + \sum_{k \neq j} \hat{V}_{jk} \tag{2.1}$$

where $\hat{H}_0$ is the atomic hamiltonian. Consider the atomic eigenfunction $|\psi_j\rangle$ and the relative eigenvalues, E_j:

$$\hat{H}_0|\psi_j\rangle = E_j|\psi_j\rangle \qquad ; \qquad \langle\psi_i|\psi_j\rangle = \delta_{ij} \tag{2.2}$$

E_j will vary randomly in the lattice.

A solution to the Equation (2.1) can be searched in the form of a superposition of stationary atomic eigenfunctions $|\psi_j\rangle$, with different probability density:

$$|\psi\rangle = \sum_i a_i|\psi_i\rangle \tag{2.3}$$

It can be shown [32] that, if the stocastic potential is sufficiently strong,

stationary localized states exist. The electron wave function can be written in the form

$$\psi(\vec{r}) = e^{-a|\vec{r}-\vec{r}_0|}\phi(\vec{r}) \tag{2.4}$$

where the wave function is localized at the point $\vec{r}_0$, with a localization lenght a.

2.1.2 Mott Law and Variable Range Hopping

At sufficiently low temperatures, the conduction in doped semiconductors is due to hopping from states whose energies lie in a narrow band (of width ϵ_0) around the Fermi level.

The conductivity of the semiconductor will be proportional to the probability that a charge carriers makes a hop between 2 localized states (close to the Fermi level).

Let's calculate the probability of hopping of one charge carrier from the state i to the state j; the hop defines either the ϵ_{ij} energy separation between the states or the lenght r_{ij} of the hop itself; hence the probability will be the product of the probability of the hop concerning the energy separation between states i and j, and the probability due to the distance between the 2 bound states.

Since the wave function of a charge carrier is localized around a donor (acceptor) site, with a localization lenght a, Equation (2.4), the probability can be expressed as

$$P_{ij} \propto \exp(-\frac{\epsilon_{ij}}{kT}) \exp(-2\frac{r_{ij}}{a}) \tag{2.5}$$

We expect the energy of the states involved in the hopping process to be very close to the Fermi level ; hence

$$\begin{aligned} |\epsilon_i - \mu| &< \epsilon_0 \\ |\epsilon_{ij}| &< 2\epsilon_0 \end{aligned} \tag{2.6}$$

Provided that the density of states per unit volume does not vanish at the Fermi energy $g(\mu) \neq 0$, the density of states might be considered constant in the narrow band involved in the hopping process (i.e. $g(\epsilon) = g(\mu)$), and the number of charge carriers per unit volume in the band is:

$$n = \int_{\mu-\epsilon_0}^{\mu+\epsilon_0} g(\epsilon)d\epsilon = g(\mu)2\epsilon_0 \tag{2.7}$$

In the hypothesis that the impurities are randomly distributed in the lattice, they will not have any spatial correlation and the average separation between sites will be proportional to $n^{-1/3}$.

Let's substitute in Equation (2.5) to r_{ij} the average of the distance between impurities, and to ϵ_{ij} the value $2\epsilon_0$ (as suggested by Equation (2.6)). We obtain:

$$P \propto \exp - \left(\frac{1}{(g(\mu)2\epsilon_0)^{\frac{1}{3}}a} + \frac{2\epsilon_0}{kT} \right) \tag{2.8}$$

Maximizing the probability of the hopping, Equation (2.8), with respect to the width of the band ϵ_0, we find the dependence of ϵ_0 from temperature:

$$\epsilon_0(T) = \frac{(kT)^{3/4}}{(g(\mu)a^3)^{1/3}} \tag{2.9}$$

Hence the band width is decreasing with temperature.

By sostitution of Equation (2.9) in Equation (2.8) we can obtain the form of the electrical conductivity of the semicondutor:

$$\sigma = \sigma_0 \exp\left(- \left(\frac{T_0}{T} \right)^{1/4} \right) = \rho^{-1}$$
$$\rho = \rho_0 \exp\left(\frac{T_0}{T} \right)^{1/4} \tag{2.10}$$

where Equation (2.10) is known as Mott Law.

A peculiarity of the hopping conduction described by the Mott Law is the average hopping lenght, which is dependent from the temperature, and can be obtained, by substitution of Equation (2.9) in $n^{-1/3}$ (Equation (2.7)),

$$\lambda = n^{-1/3} = a \left(\frac{T_0}{T} \right)^{1/4} \tag{2.11}$$

in particular we note that the hopping lenght tends to increase as T decreases; for this reason this mechanism of conduction is named Variable Range Hopping.

2.1.3 Coulomb Gap

The derivation made in the previous paragraph results from the hypothesis of a non vanishing density of states of charge carriers around the Fermi energy.

On the other hand, for a crystalline doped semiconductor, studies on interaction between localized electrons show that the density of states must have a minimum at the Fermi level [33, 34]; i.e. the filled and empty states are separated by an energy gap Δ.

Hence, we consider now the form of the temperature dependance of hopping conductivity resulting from a vanishing density of states, $g(\epsilon)$, at the Fermi energy.

Pollak and Hamilton [33] considered the case when the density of states decreases according to a power law of the form:

$$g(\epsilon) = g' \left(\frac{|\epsilon - \mu|}{\epsilon'} \right)^m \tag{2.12}$$

Calculating the probability of a hop (Equation (2.8)), using the density of states of Equation (2.12) in Equation (2.7), we obtain in a straightforward way, a generalized form of Equation (2.10):

$$\rho = \rho_p \exp \left(\frac{T_p}{T} \right)^p \tag{2.13}$$

$$\text{where } p = \frac{m+1}{m+4} \tag{2.14}$$

It is worth noting that, in the case of constant density of states, $m = 0$, and $p = 1/4$, as deduced by Mott (§(2.1.2)).

The Coulomb interaction between charge carriers in the hopping regime can lead to a density of states that vanishes at the Fermi level as a parabola[33] (i.e. $m = 2$ in Equation (2.7)). This energy gap at the Fermi level is known as Coulomb gap. In such case the resulting generalized Mott law (Equation (2.13)) is

$$\rho = \rho_{\frac{1}{2}} \exp\left(\frac{T_{\frac{1}{2}}}{T}\right)^{1/2} \tag{2.15}$$

2.2 Ultra Low-Temperature non linearity

Electrical resistivity dominated by the hopping mechanism, and described by Equation (2.13) is found to be valid in a rather large temperature range.

On the other hand, it has been reported in literature (see for instance [35, 36, 37, 38, 39]) that at very low temperature, a non Ohmic behaviour appear. Such non linearities tend to increase as temperature is lowered, Figure (2.1). This behaviour can be due to either thermal or electrical field effects. Moreover, one can desume by $P = V^2/R$ that

$$E = \sqrt{\rho P / v} \tag{2.16}$$

where E is the electrical field, P is the power, v is the volume of the sample and ρ the resistivity. Hence, it is not easy to a priori distinguish from electric-field effect, to power density (thermal) effect, on the non Ohmic behaviour of the resistivity.

A few models have been proposed to explain the non Ohmic behaviour; they are models that rely on the electric field effect and a thermal model, hot electron model.

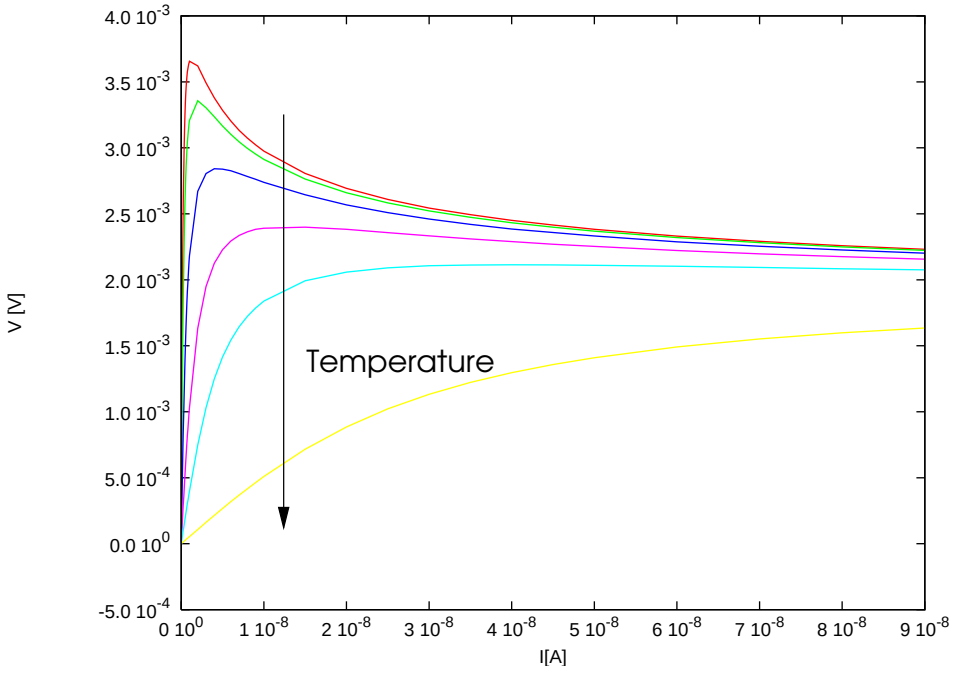

Figure 2.1: Tipical non linearity of a NTD sample; the non linearity effect is increasing as the temperature is decreasing. The arrow indicates the direction of the increase of the temperature.

2.2.1 Field Effect Models

There are several different analytic predictions for this effect. Considering the case in which the semiconductor follows the Mott law Equation (2.10) (hence with $n = 1/4$), and considering the motion of charge carriers both along and against the electric field, Hill [40] obtained a dependance for the current density j on the electrical field E:

$$j(T,E) \propto \sigma(T,0)E \sinh\left(C\frac{eE\lambda}{kT}\right) \tag{2.17}$$

where e is the electron charge, λ is the hopping lenght (Equation (2.11)) and C a constant. At sufficiently high E fields (i.e. $eE\lambda \gg kT$) the reverse current can be ignored; in this case

$$j(T,E) \propto \sigma(T,0)E \exp\left(C\frac{eE\lambda}{kT}\right) \tag{2.18}$$

$$\rho(T,E) = \rho(T,0)E^{-1} \exp\left(-C\frac{eE\lambda}{kT}\right) \tag{2.19}$$

Other authors [40] have derived the same Equations (2.17,2.19) in the hypothesis that in the Ohmic region the semiconductor follows Equation (2.13) in the case of a Coulomb gap ($n = 2$ or $p = 1/2$) [36, 41].

2.2.2 Hot Electron Model

The origin of the low temperature non linearity can be described with a purely thermal empirical model: the Hot Electron Model (HEM).

In this model a lattice with charge carriers (as a semiconductor in hopping regime as well as a metal) is described by 2 interacting subsystems: electrons (charge carriers) and phonon (lattice).

The strenght of the interaction is dependent on temperature, and actually it is decreasing with it. This is quite obvious because the interaction of an electron with a phonon is proportional to the number of final states that

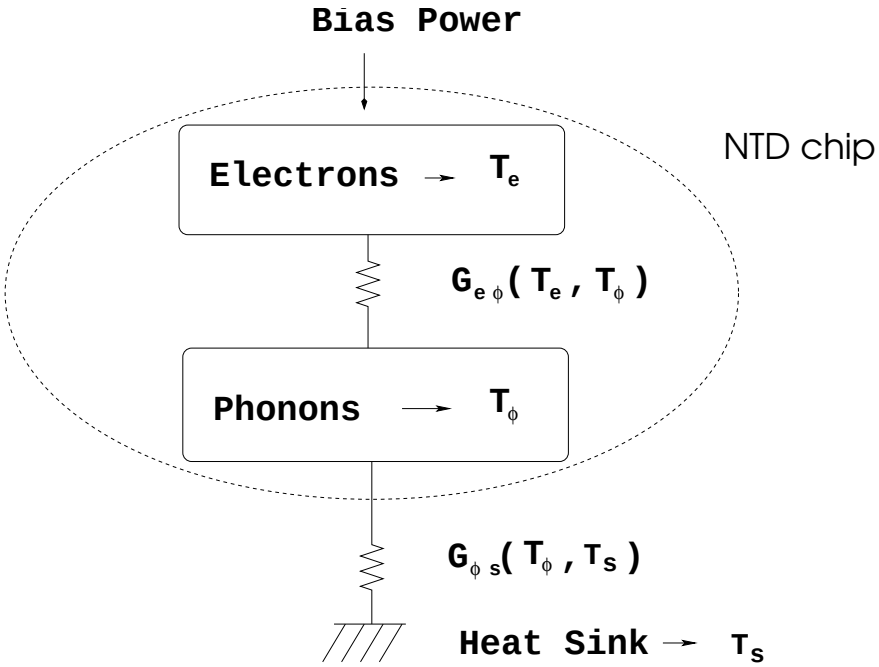

Figure 2.2: Schematic of Hot Electron model

electrons and phonon can occupy, and the number of final states available for the electrons is decreasing with temperature.

At sufficiently low temperatures, the interaction between the two subsystems can be so weak that there is no thermal equilibrium between them, and the energy is distributed among electrons more rapidly than it is distributed to the lattice, resulting in a different temperature for electron and phonon subsystems.

The interaction between the two subsystem in the HEM is represented by means of a thermal conductance $G_{e\phi}$ Figure (2.2). In the next paragraph we will see how is possible to calculate the analytic form of the thermal conduction $G_{e\phi}$ for a metal.

HEM in metals

The Hot Electron effect it is very well known in metals and it has been calculated [42, 43, 31]. The physical process that is the origin of the hot

electron effect is the lowering of the emission/absorption rate of phonon by electrons. The total thermal conductivity between the two systems is deduced by calculating the net power, $P = P_{\text{emission}} - P_{\text{absorption}}$, transmitted between the electrons, at temperature T_e, and phonons, at temperature T_ϕ.

The phonon emission rate (as well as the absporption rate) can be deduced by the Fermi golden rule:

$$\tau^{-1}_{\mathbf{k}\mathbf{k}'} = \frac{2\pi}{\hbar}|M|^2\delta(E_{\mathbf{k}} - E_{\mathbf{k}'} - \epsilon_{\mathbf{q}})(1 - f(E_{\mathbf{k}'}))(n(\mathbf{q}) + 1)) \tag{2.20}$$

where $f(E_{\mathbf{k}})$ is the Fermi-Dirac distribution, $n(\mathbf{q})$ is the Bose-Einstein distribution (phonons are bosons), $|M|^2$ is the coupling matrix element, and $\epsilon_{\mathbf{q}} = \hbar v_s q$ is the dispersion relation for the phonon (v_s is the speed of sound).

The power P_{emission} is calculated by multiplying the Equation (2.20) by the energy of emitted phonons, $\epsilon_{\mathbf{q}}$, and summing over the total electron initial states (indicated by k) and the total possible states of emitted phonons:

$$P_{\text{emission}} = \Sigma_{\mathbf{k}'} f(E_{\mathbf{k}'}) \Sigma_{\mathbf{q}} \epsilon_{\mathbf{q}} \tau^{-1}_{\mathbf{k}\mathbf{k}'}$$

$$P_{\text{emission}} = \int_0^\infty f(E_{\mathbf{k}'}) g_e(E_{\mathbf{k}'}) dE_{\mathbf{k}'} \int_0^\infty \epsilon_{\mathbf{q}} \tau^{-1}_{\mathbf{k}\mathbf{k}'} g_\phi(\epsilon_{\mathbf{q}}) d\epsilon_{\mathbf{q}} \tag{2.21}$$

where we introduced the integral form by means of the density of states of electrons, $g_e(E)$, and phonons, $g_\phi(E)$, respectively.

The same process can be made for the absorbed phonon, leading to:

$$\tau^{-1}_{\mathbf{k}\mathbf{k}'} = \frac{2\pi}{\hbar}|M|^2\delta(E_{\mathbf{k}} - E_{\mathbf{k}'} - \epsilon_{\mathbf{q}})(1 - f(E_{\mathbf{k}'}))(n(\mathbf{q}))) \tag{2.22}$$

$$P_{\text{absorption}} = \int_0^\infty f(E_{\mathbf{k}'}) g_e(E_{\mathbf{k}'}) dE_{\mathbf{k}'} \int_0^\infty \epsilon_{\mathbf{q}} \tau^{-1}_{\mathbf{k}\mathbf{k}'} g_\phi(\epsilon_{\mathbf{q}}) d\epsilon_{\mathbf{q}} \tag{2.23}$$

The detailed calculation was given by Hill [42] who integrated Equation (2.21) and Equation (2.23) obtaining the following form of the power flowing between electrons and phonons:

$$P = \xi V \left(T_e^5 - T_\phi^5\right) = \int_{T_\phi}^{T_e} k_{e\phi}(T')dT' \tag{2.24}$$

where ξ is a constant independent of volume and temperature, V is sample volume.

From Equation (2.24) we can deduce, now in a straightforward way, the temperature dependance of electron-phonon thermal conductivity for metals:

$$k_{e\phi}(\text{metals}) \propto T^4 \tag{2.25}$$

Such a behaviour has been first reported in literature by Anderson and Peterson [43].

HEM in VRH semiconductor

We note that the situation of a semiconductor in the hopping regime is quite different from that of metals, where electrons are free to move; nevertheless the same Equation (2.21) and Equation (2.23) still hold.

Since density of states for the electrons is not well known for doped semiconductors, it will not be possible to obtain an analytic derivation of Equation (2.21) and Equation (2.23) leading to Equation (2.24). Anyway it is reasonable to think that the expression of P for a doped semiconductor is similar to that of metals, Equation (2.24). Because of this arbitrary assumption we call the HEM an empirical model.

Resuming the characteristics of the hot electron model we point out that it is based on four assumption:

1. the charge carriers (either electron or hole) are at thermodinamic equilibrium, hence a temperature, T_e, of the subsystem can be defined;

2. the T_e can be measured by means of Equation (2.13):

$$\rho = \rho_p \exp\left(\frac{T_p}{T_e}\right)^p$$

3. the bias power is totally deposited in the electron subsystem;

4. the thermal conductivity between electrons and phonons, $k_{e\phi}(T)$ has a power law temperature dependance (as can be calculated for metals):

$$k_{e\phi}(T) = (\beta + 1)\ g_{e\phi}\ T^{\beta} \quad [\mathrm{W/K^2}] \tag{2.26}$$

where β and $g_{e\phi}$ are constants that do not depend on temperature.

2.3 Influence of Magnetic Field

In this section we will investigate the properties of doped semiconductors in the VRH regime, when a magnetic field is superimposed. A rigorous treatment of the problem can be found in [33]; we will present here a rather naive theory that accounts for most of the electrical properties.

The effect of applying a magnetic field to a semiconductor in the hopping regime is that a giant positive magnetoresistance shows up. Anyway, also negative magnetoresistance are reported in literature [44].

2.3.1 A naive theory

As for the case of the Hall-effect, when a magnetic field is applied to a semiconductor the charge carriers are moved, in the lattice, orthogonally to their velocity. As a final effect, the lattice can be regarded as made by equipotential surfaces in which a charge carrier can freely move, but cannot (easily) exit. Hence, we may think the semiconductor in magnetic field as made by layers of 2D lattices as shown in Figure (2.3).

In this naive vision, we can redo the calculations done in §(2.1.2) and in §(2.1.3) to determine what is the behaviour of the sample: the 2D-Mott Law, in both cases when the density of states is constant at the Fermi level, and when it is vanishing at the Fermi level with a power law (Equation (2.12)).

Let's, then, follow the same steps: the electrical conductivity of the sample is proportional to the probability that a charge carrier has to make the hop, Equation (2.5)

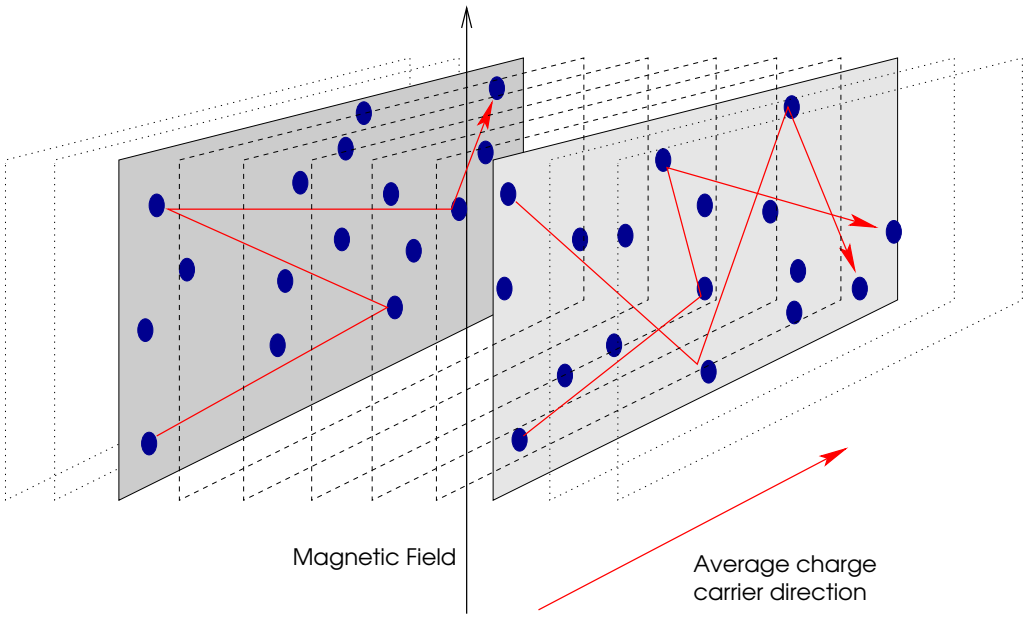

Figure 2.3: the lattice can be regarded as made by equipotential surfaces in which a charge carrier can move by VRH hopping (red lines), but cannot exit. The donor sites (in blue) are randomly distributed in the lattice. The crystalline lattice is not shown.

$$P_{ij} \propto \exp(-\frac{\epsilon_{ij}}{kT}) \exp(-2\frac{r_{ij}}{a})$$

The number of charge carrier per unit surface (2D model) will be expressed again by Equation (2.7)

$$n = \int_{\mu-\epsilon_0}^{\mu+\epsilon_0} g(\epsilon) d\epsilon$$

We can write Equation (2.8) in this case as

$$P_{2D} \propto \exp\left(-\left(\frac{1}{n^{\frac{1}{2}}a} + \frac{2\epsilon_0}{kT}\right)\right) \tag{2.27}$$

the main difference from the 3D lattice to the 2D is that the average hopping lenght, Equation (2.11), is not anymore proportional to $n^{1/3}$ but to $n^{1/2}$, and that the density of states is expressed per unit surface instead of per unit volume; henceforth the expression $n^{\frac{1}{2}}a$ is dimensionless.

By maximization of Equation (2.27) with respect to the bandwidth ϵ_0, and in the hypothesis that the density of states has the form of Equation (2.12)

$$g(\epsilon) = g' \left(\frac{|\epsilon - \mu|}{\epsilon'} \right)^m$$

again we find a form of the resistivity expressed as a generalized Mott law Equation (2.13); in particular we find that

$$\rho = \rho_p \exp \left(\frac{T_p}{T} \right)^p \tag{2.28}$$

$$\text{where } p = \frac{m+1}{m+3} \tag{2.29}$$

We can distinguish, now, between the two cases in which the density of states vanishes, and the case in which it has a minimum at the Fermi level. For a constant density of states we have that m must be equal to 0, i.e. $m = 0$ that leads to $p = 1/3$. In the important case in which a coulomb interaction between charge carriers plays a significant role, the density of the states has a minimum as a parabola at the Fermi level, i.e. $m = 2$ and subsequently $p = 3/5$.

We must stress that Equation (2.28) is exactly the same obtained by Shklovskii and Efros [33] with a rigorous derivation for a 3D model. It is worth to note that indeed the Equation (2.28) contains a kind of dependence from the magnetic field in the constant $T_p = T_p(H)$. As a matter of fact in the derivation of Equation (2.28) we assumed a certain density of charge carriers in the layer. This density is both field dependent and spatially dependent (Hall effect).

Shklovskii and Efros provide also a relation linking the parameter T_p to the magnetic field, when p is equal to 1/3:

$$T_{1/3}(H) \propto H \tag{2.30}$$

2.3.2 Magnetoresistance

A characteristic feature of the hopping mechanism of conduction is a gigantic positive magnetoresistance which depends exponetially on the strenght of the magnetic field. Such magnetoresistance has been observed by various authors; for a detailed review see [33].

It is well accepted [45, 46, 47] that the magnetoresistance of a VRH semiconductor has the form

$$\ln\left(\frac{\rho(T,H)}{\rho(T,H=0)}\right) = \left(\frac{B}{B_0}\right)^{\xi} \tag{2.31}$$

At low fields, the parameter ξ is expected to be $\xi = 2$ [33, 46]; in the high field limit, ξ should ultimately decrease to a value of $1/3$ for a constant density of states, or to $1/5$ for a Coulomb gap[46]. One can see that all theoretical models predict values of ξ less than unity [33]. Nevertheless, authors report experimental values of $\xi \approx 1$ [46].

The nature of the gigantic magnetoresistance was elucidated as early as 1958 [48]. As is well known, in a strong magnetic field the wave functions of impurity electrons are squeezed in the transverse direction. In the simplest case, when the wave functions are spherically symmetric in the absence of magnetic field, they become cigar-shaped. This leads to a sharp decrease in the overlap of the wave function tails, and hence to an exponentially increased resistivity. An exponential positive magnetoresistance is usually an unanbiguous evidence of the importance of the tails of the wave functions, and can be regarded as a proof of the hopping mechanism of conduction of the material under study.

Chapter 3

Experimental apparatus

3.1 The Refrigerator

In this section we will show the principles of work of the dilution refrigerator. The Dilution Refrigerator is a refrigerator that can reach temperatures as low as about 2 mK (1.85 mK is the world record) depending from various factors we will take into account.

First of all we will describe the cooling process §(3.1.1) and §(3.1.2) and then we will describe how a dilution refrigerator is made §(3.1.3).

3.1.1 Properties of ^{3}He-^{4}He mixture

In figure 3.1 phase diagram of liquid ^{3}He-^{4}He at saturated vapour pressure is shown. The X axis represents the molar fraction of ^{3}He in the mixture and the Y axis represents the temperature. Let us consider some features of this mixture.

Above 0.87 K ^{3}He can be diluted in ^{4}He in any concentration. Superfluid transition of pure ^{4}He occurs at 2.177 K, while for pure ^{3}He occurs at a temperature of about 2 mK (depending on the magnetic field). The effect of mixing the two He isotopes is that the superfluid phase transition shifts from 2.177 K of pure ^{4}He to lower values; this effect is shown in Figure (3.1)

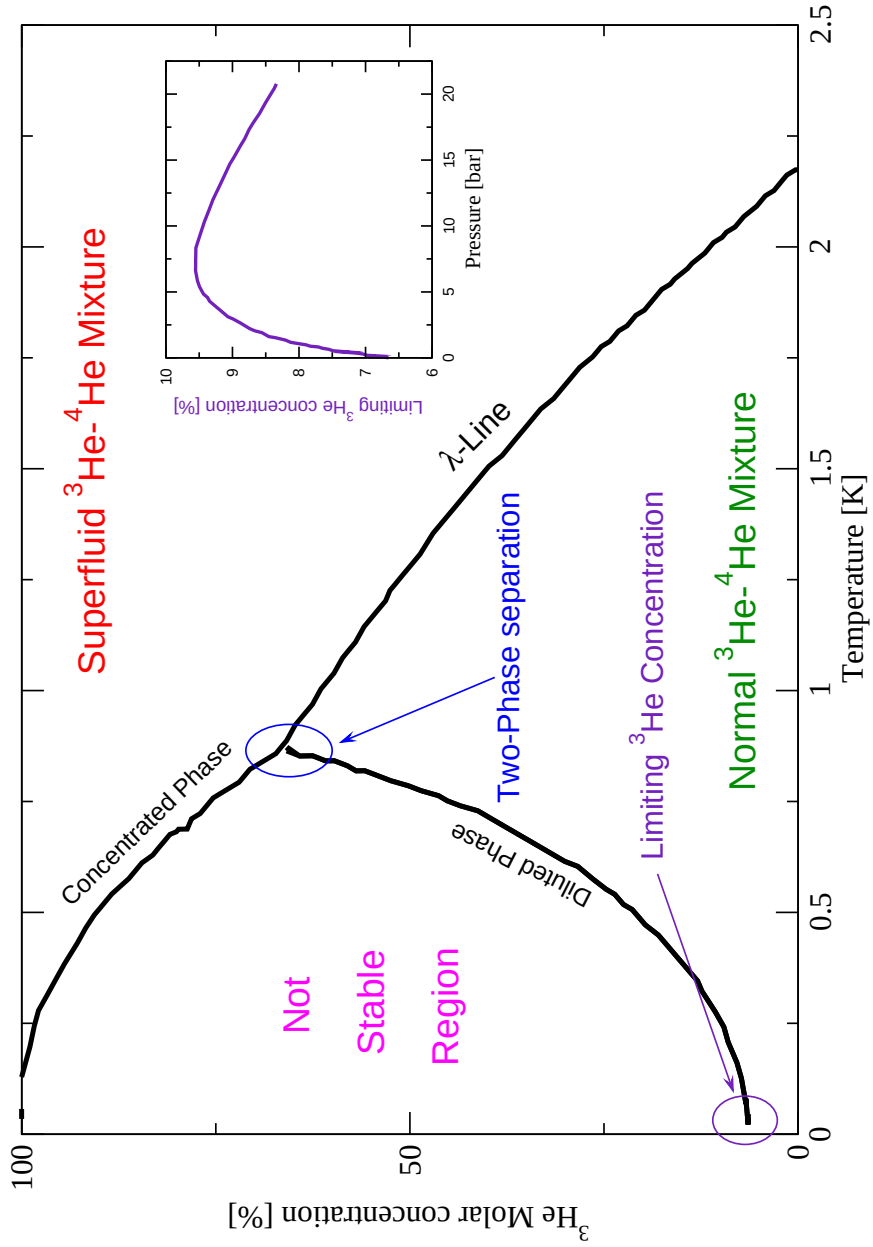

Figure 3.1: Phase diagram of ^{3}He-^{4}He mixture as a function of temperature in saturated vapour pressure. In the inset it is shown the limiting concentration of ^{3}He in ^{4}He at T = 50 mK as a function of pressure.

where the λ-line represent the superfluid phase transition..

Anyway, below 0.87 K, at saturated vapour pressure, the mixture is not stable for some ^{3}He molar concentrations, resulting in a two phase equilibrium. One phase will be consisting of almost pure ^{3}He and the other in almost pure ^{4}He. The ^{3}He rich phase will be floating over the ^{4}He rich phase, because of the density ratio.

One remarkable feature of the two-phase region is that the ^{3}He rich phase consists in almost 100% pure ^{3}He while in the ^{4}He rich phase (Dilute phase) ^{3}He can always be diluted in concentrations that vary with pressure as shown in figure.

At low pressures (P $<$ mbar) the dependence of ^{3}He concentration in the dilute phase is very weak and it can be considered constant. In this way the concentration of ^{3}He in the dilute phase is function only of temperature [31]:

$$x = 0.065(1 + 10T[K]^2) \tag{3.1}$$

3.1.2 Cooling by dilution of ^{3}He in ^{4}He

If you force, at constant pressure, n mols of ^{3}He atoms to pass from the concentrated phase to the diluted one you must give an energy Q

$$Q = T\Delta S = nT(S_d - S_c) \tag{3.2}$$

where S_c and S_d are the entropy of ^{3}He in the concentrated and diluted phase.

If the transition of the atoms from one phase to the other is slow enough we can consider the transition reversible and

$$dS = \frac{CdT}{T}$$

where C represents the heat capacity.

So one can write Equation (3.2) in the following way

$$Q = nT \int_c^d dS = nT \int_c^d \frac{CdT}{T}$$

We can calculate the integral from the initial state (atoms in the concentrated phase) to the final state (atoms in the diluted phase) using any arbitrary path with the same beginning and end. So we will choose a path that starts at a temperature T in the concentrated phase, goes to $T = 0$ and goes back to T in the diluted phase. In this way $S_c(0) = S_d(0) = 0$.

$$Q = nT \left(\int_0^T \frac{C_d(T')dT'}{T'} - \int_0^T \frac{C_c(T')dT'}{T'} \right) \tag{3.3}$$

where C_d is the heat capacity of ^{3}He in the diluted phase, and C_c is the heat capacity of ^{3}He in the concentrated phase.

Experimentally, the heat capacitances below 50 mK of ^{3}He in concentrated phase and diluted phase are found to be linear with temperature [31]

$$C_c(T) = 25\ T \quad [\text{J/mol K}] \tag{3.4}$$

$$C_d(T) = 107\ T \quad [\text{J/mol K}] \tag{3.5}$$

The integral in eq 3.3 is then strightforward

$$Q = nT\,(C_dT - C_cT) = n(C_d - C_c)T^2 = n82\ T^2 \quad [\text{J}]$$

when n is expressed in mol and T in K.

Since Q is positive the transition from concentrated phase to diluted phase absorbs energy.

If we force a constant number of mols n to make the transition from concentrated phase to the diluted phase per unit time, the transition will absorb an energy per unit time $Q/\Delta t$, which is equivalent to say that the process has a cooling power of

$$P = \frac{Q}{\Delta t} = \frac{n}{\Delta t} 82\ T^2 \quad = \dot{n}\ 82\ T^2\ [\text{W}] \tag{3.6}$$

where $\dot{n}$[mol/s] is the ^{3}He flow.

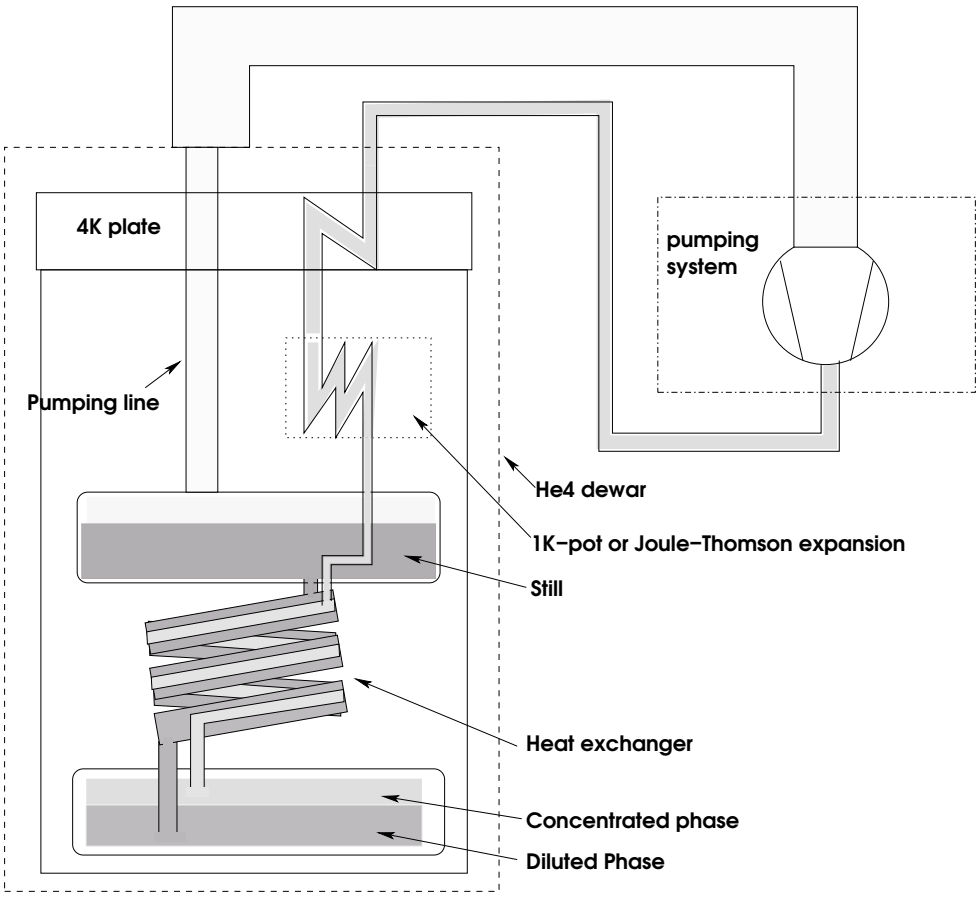

Figure 3.2: Conceptual view of a dilution refrigerator.

3.1.3 Scheme of a Dilution Refrigerator

The remarkable feature of the dilution refrigerator is that it is a closed cycle refrigerator, which can work virtually forever. The mixture is circulated in the refrigerator by means of pumps and compressors working at 300K.

To be able to exploit the effect of cooling by dilution of ^{3}He in ^{4}He it is due to take the mixture down to a temperature where the separation of phases happens; this is obtained by means of 4 main cooling steps.

In Figure (3.2) a schematic view of a dilution refrigerator, together with the pumping system is shown. We will refer to "dilution unit" indicating the part of the scheme including the mixing chamber, the heat exchangers, the

T [K]	P(^{3}He) [mbar]	P(^{4}He) [mbar]
0.40	$2.86\ 10^{-3}$	$7.00\ 10^{-6}$
0.50	$1.05\ 10^{-2}$	$1.10\ 10^{-5}$
0.55	$1.73\ 10^{-2}$	$5.60\ 10^{-5}$
0.60	$2.55\ 10^{-2}$	$2.25\ 10^{-4}$
0.65	$3.61\ 10^{-2}$	$6.92\ 10^{-4}$
0.70	$4.81\ 10^{-2}$	$1.80\ 10^{-3}$
0.75	$6.24\ 10^{-2}$	$4.30\ 10^{-3}$
0.80	$7.70\ 10^{-2}$	$8.60\ 10^{-3}$
0.85	$9.50\ 10^{-2}$	$1.50\ 10^{-2}$
0.90	$1.03\ 10^{-1}$	$3.00\ 10^{-2}$
1.00	$1.50\ 10^{-1}$	$7.52\ 10^{-2}$
1.20	$2.03\ 10^{-1}$	$2.03\ 10^{-1}$

Table 3.1: Saturated vapour pressure of ^{3}He and ^{4}He at different temperatures.

still.

First of all, the dilution refrigerator is put in a vacuum chamber dipped in liquid He, hence, it is in 4 K ambient (main bath). The first step is, then, to take the mixture from 300 K to 4 K by a proper thermalization with the He bath vapours, and with the liquid He bath.

The second step is to further cool down the mixture at about 1.5 K by means of a ^{4}He evaporation refrigerator (usually indicated as 1K-pot), or by means of a Joule-Thomson expansion. The use of a 1K-pot is a little bit more complicated than the latter because one must fill the 1K-pot countinuously by means of a capillar put in the main bath, but the cooling power of a 1K-pot can be larger than the cooling power of a Joule-Thomson expansion stage. At the temperature of 1.5 K the mixture gets liquid and begin to condense in the dilution unit filling first the mixing chamber, and then the still.

When liquid mixture is present in the still, it behaves as an evaporator in which both ^{3}He and ^{4}He are pumped away. In Table(3.1) are reported the

saturated vapour pressures of ^{3}He and ^{4}He; it is evident that at sufficiently low temperatures (below 750 mK) the vapour pressure of the ^{3}He is more than one order of magnitude larger than that of ^{4}He, hence the gas evaporated from the still is almost composed by ^{3}He. So the still behaves as a pumped ^{3}He refrigerator, which is capable to reach temperatures down to 300 mK. By keeping the temperature of the still around 700 mK the flux of evaporated ^{3}He is kept large, as its cooling power.

Further cooling is obtained by means of counterflow heat exchangers, in which the incoming ^{3}He is cooled by the diluted phase, down to temperatures close to the mixing chamber temperature as much as possible.

The optimum ratio of the mixture is mostly determined by the geometry of the dilution refrigerator and is calculated to have the phase separation inside the mixing chamber.

3.2 Termometry

In this section we will see how to measure temperature and what kind of thermometers we have used in this work.

Thermometers are divided into two categories: primary thermometers and secondary thermometers. The first being the one whose releation between thermometrical property involves only temperature and fundamental constants, the latter being those devices in which the thermometrical property does involve some device dependent parameter, as well. The secondary thermometers need to be calibrated with respect to primary thermometers.

Primary low temperature thermometers are mainly noise thermometers, nuclear orientation emission thermometers, magnetic thermometers (Coulomb blockade []) and ^{3}He fusion curve cells. The use of such devices is not straightforward and it is generally done in metrological institutes. Secondary thermometers, mainly resistance thermistors (§(2.1.2)) or capacitance thermometers [49], on the other hand, are much easier to use.

In our laboratory we have:

- two superconducting fixed point devices;
- one calibrated RuO_2 thermometer;

3.2.1 Fixed points devices

A rather simple way to disseminate temperature points is to exploit the superconducting transition of bulk or thin layer material. When a material becomes superconducting its magnetic properties change abruptly. Hence the superconducting transition changes the mutual inductance of two coils the sample is put into. Care must be payed in order to shield the sample from external magnetic field that can shift the transition temperature.

NIST 767 A fixed point reference device, is certified by the National Institute of Standards & Technology, and it is a set of 6 bulk materials with a superconducting transition between 9.20860 K (Nb) and 0.52005 K (Cd).

SRD1000 fixed points reference device, is made by HLC and contains a set of 10 thin layer samples, whose transitions ranges from 1.1K (Al) to 15 mK (W).

This kind of thermometers are obviously sensible only at the transition temperatures of the samples, and hence are mostly useful as reference, to calibrate other thermometers whose thermal properties varies continuosly with the temperature.

3.2.2 Resistance termometry

Resistance thermometry is based on the steep dependence of the electrical resistance of doped semiconductors on temperature, as seen in §(2.1.2). The measurement of temperature is done by measuring the resistance of a calibrated thermistor. The calibration of each thermistor is done with respect to our reference secondary resistance thermometer [1] in the range 26–1100

[1] Calibrated with respect to ITS 90 (International Temperature Scale 90) by Dr. K. Uhlig of Walter Meissner Institute für Tieftemperatureforshung (Munich)

mK; the enlargement of the calibration range of our thermometers is made by means of NIST 767A and SRD1000 superconducting reference devices.

The measurement of the resistance of the thermistors is made in a four probe configuration by means of AC resistance bridges, or by DC measurements. In our laboratory we have 3 kinds of resistance AC bridges:

- AVS-47 by Elettroniika Oy: square wave, configurable frequency.
- LR-700 by Linear Research: sinusoidal wave 15.9 Hz.
- Barras Provence ORPX: square wave 28 Hz.

This kind of resistance bridges are able to measure the resistance dissipating a very low power (down to about 10^{-14} W) on the thermistor, in order not to heat it up. The measurable resistance ranges from few tens of Ω to a few hundreds of kΩ. Moreover the AC bridge is quite fast: the measurement refresh rate is about 2–4 Hz.

The DC resistance measurement is done by using a Keythley 236 current source, capable to circulate currents down to 10^{-15} A, and a Keythley multimeter model 2000. With these two instruments we can cover the range that the AC bridges cannot explore: resistances from about one kΩ to hundreds of MΩ.

DC measurements, on the other hand, are very slow because, in order to reduce errors, a large number of samples is aquired, and to get rid of parasitic voltage across the thermistor we have to bias the thermistor with $+I$ and $-I$, §(5.1.2).

Part II

Measurements on NTD-Germanium

Chapter 4

Electrical Conductivity

In this chapter we report about the production, §(4.1), of various samples of NTD Ge for the CUORE experiment.

In §(4.2) we describe the experimental set-up used for the measurement of the ultra-low-temperature electrical conductivity of such samples. Comparison with data present in literature and theory is presented in §(4.3).

4.1 NTD technique

Neutron Transmutation Doped germanium is produced by irradiating an ultrapure Ge crystal by means of a flux of thermal neutrons. Ge nuclei capture the neutrons and form various radioactive Ge isotopes, which subsequentely decay into As, Se and Ga [39, 50, 51, 52]. As shown in table 4.1, due to the isotopical composition of Ge and to the neutron cross section, the resulting doping is of p-type.

The dopant concentration depends both on the natural abound and on neutron absorption cross section. For natural Ge, the following dopant concentrations per neutron unit flux are obtained [51]:

$$[\mathrm{Ga}] = 2.94 \;\; 10^{-2}\mathrm{cm}^{-3} \text{ per neutron/cm}^2\text{/s} \tag{4.1}$$

Isotopical fraction	Reaction	σ(barn)	$\tau_{1/2}$	Type
20.5%	$^{70}_{32}$Ge(n,γ)$^{71}_{32}$Ge $\rightarrow^{71}_{31}$Ga +K	3.25	11.2 d	p
36.5%	$^{74}_{32}$Ge(n,γ)$^{75}_{32}$Ge $\rightarrow^{75}_{33}$As +β^-	0.52	82.8 min	n
7.8%	$^{76}_{32}$Ge(n,γ)$^{77}_{32}$Ge $\rightarrow^{77}_{33}$As + β^- $\rightarrow^{77}_{34}$Se + β^-	0.16	11.3 h	n

Table 4.1: Induced nuclear decays for neutron absorbtion in ^{70}Ge, ^{74}Ge and ^{76}Ge isotopes.

$$[\mathrm{As}] = 8.37 \;\; 10^{-3}\mathrm{cm}^{-3} \text{ per neutron/cm}^2\text{/s} \tag{4.2}$$

The Se concentratation is negligible.

The NTD process has two advantages:

- Since the cross section for neutron capture is quite low, the neutron flux remains constant in passing through to sample, i.e. the doping is very homogeneus, whereas melt-doped Ge sensors show dispersive properties, even if they are cut by nearby volumes of the same chip.
- The doping process may be controlled changing the integrated flux of neutrons, making possible to approximately predict the resistivity of the thermistor as a function of temperature.

Each pure Ge sample was irradiated by a flux of thermal neutrons and then annealed at about 400°C for six hours in order to "repair" damage in the crystal structure. Electrical contacts were made by heavily doping two sides of the sample with B^+ ions ($3 \cdot 10^{14}$ cm^{-2}) to a depth of about 200 nm. A layer of Pd (about 20 nm) and one of Au (about 400 nm) are sputtered onto the two surfaces. The sample is then annealed at 250°C for one hour.

In table 4.2 are reported the NTD samples produced in the frame of the CUORE experiment. Series 33 to 38 have been doped in 1999, with increasing exposure to neutron flux, see Figure (4.1). Series 33B, 34B and 35B are series 33, 34 and 35, respectively, that received a second dose in 2001.

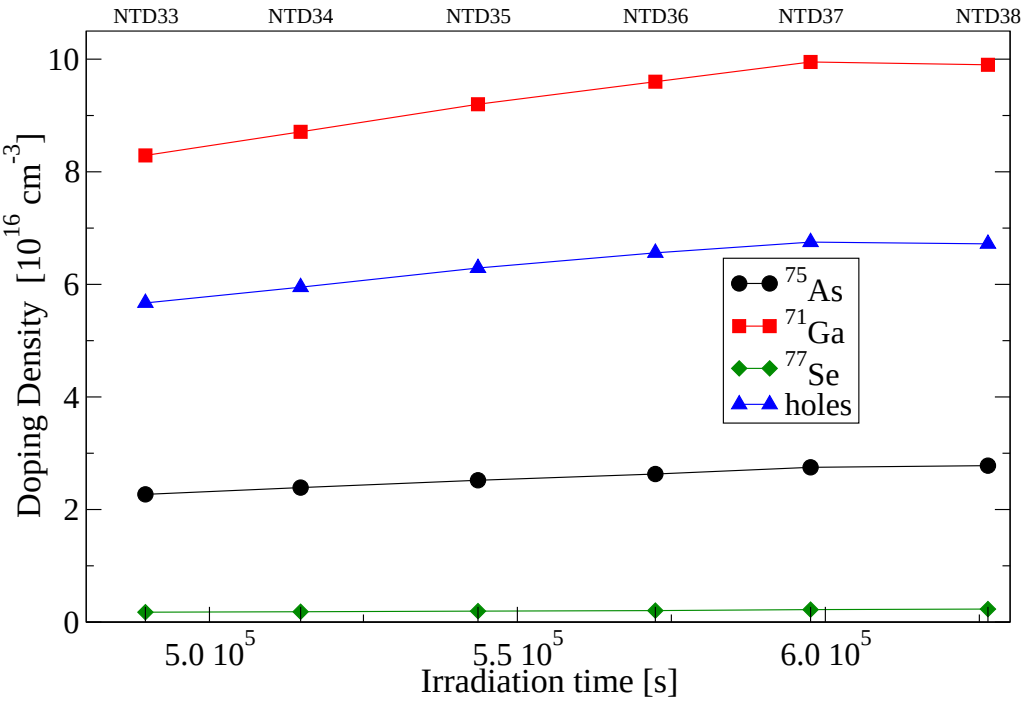

Figure 4.1: Doping density of NTD series 33 to 38, as a function of irradiation time.

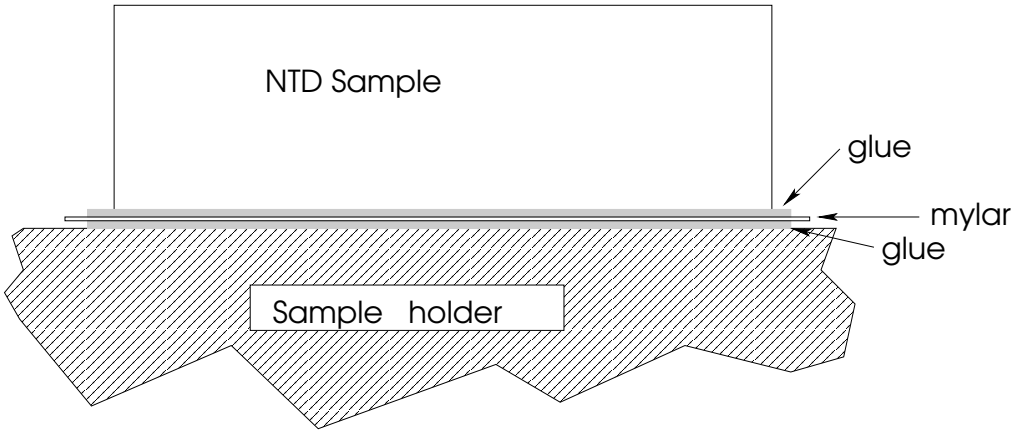

Figure 4.2: Schematic of how a NTD is glued on the copper holder in order to have both a good thermal contact and electrical insulation.

4.2 Experimental set-up

Each sample was glued, with IMI-7031 Varnish, on a copper holder in thermal contact with the mixing chamber of the refrigerator. Electrical insulation and good thermal contact between holder and sample was obtained by interposing a thin foil of mylar (4μm), Figure (4.2). The sample holder was surrounded by a copper radiation shield at the temperature of the mixing-chamber of the refrigerator.

The electrical contacts were made with two thin gold wires (50 μm in diameter, about 2 cm long) ball-bonded to each Au surface. Since a 4 probe method was used to measure the resistance of the thermistors, two manganine wires were soldered to each gold wire; the manganine wires were thermalized on the sample holder. Electrical leads from the top of the cryostat to the experiments were made by manganine twisted pairs; each electrical lead was RF filtered on the top of the cryostat in order to reduce the spurious power.

Usually two separated AC resistance bridge were used to measure the temperature and the resistance of samples, §(3.2.2). Temperature is measured by means of a calibrated RuO_2 thermistor, §(3.2).

With the RF filters the AC bridges can measure resistances up to a few hundreds of kΩ; larger resistances interfere with the RF filter impedance,

and the bridge's lock-in amplifier is not able to read correctly anymore. For this reason, a DC characteristographer has been used for resistance larger than 200 kΩ.

4.3 Results and Discussion

The results of the resistivity measurements on all the NTD samples produced for the CUORE project, are reported in Figure (4.3), where the logarithm of the resistivity is shown as a function of $1/T^{\frac{1}{2}}$; this is a way to linearize Mott law that stands when the Coulomb Gap is effective ($p = 1/2$):

$$\rho(T) = \rho_{1/2} \exp(T_{1/2}/T)^{\frac{1}{2}}$$

From the figure, it is evident that such a law fits reasonably well the data points in the whole temperature range. The slope of the curves is the parameter $T_{1/2}$ which has a dependence from the doping level. As a matter of fact, the more the doping the less the resistivity. In figure Figure (4.4) we show the $T_{1/2}$ parameter as a function of doping density; the parameter is found to decrease with the increase of the doping level, as expected.

Discussion

Although it seems that the theoretical prediction of a Coulomb Gap effect in NTD Germanium and the experimental measurements are in good agreement, systematic deviations from the expected CG Mott law (with $p = 1/2$) can be found. In Figure (4.5) we show the deviation of the fit of the generalized Mott law, Equation (2.13), from the experimental data points, in the case in which p is fixed to $1/2$, or is fitted as a variable. The $p = 1/2$ fit is, by eye, worse than the variable p one.

Recently Woodcraft et al. [53], have deeply investigated the resistivity of a few samples of NTD Germanium to compare the theory with the experimental data, focusing their attention on the p parameter. They find that the best fit to experimental data is obtained by letting the parameter p to

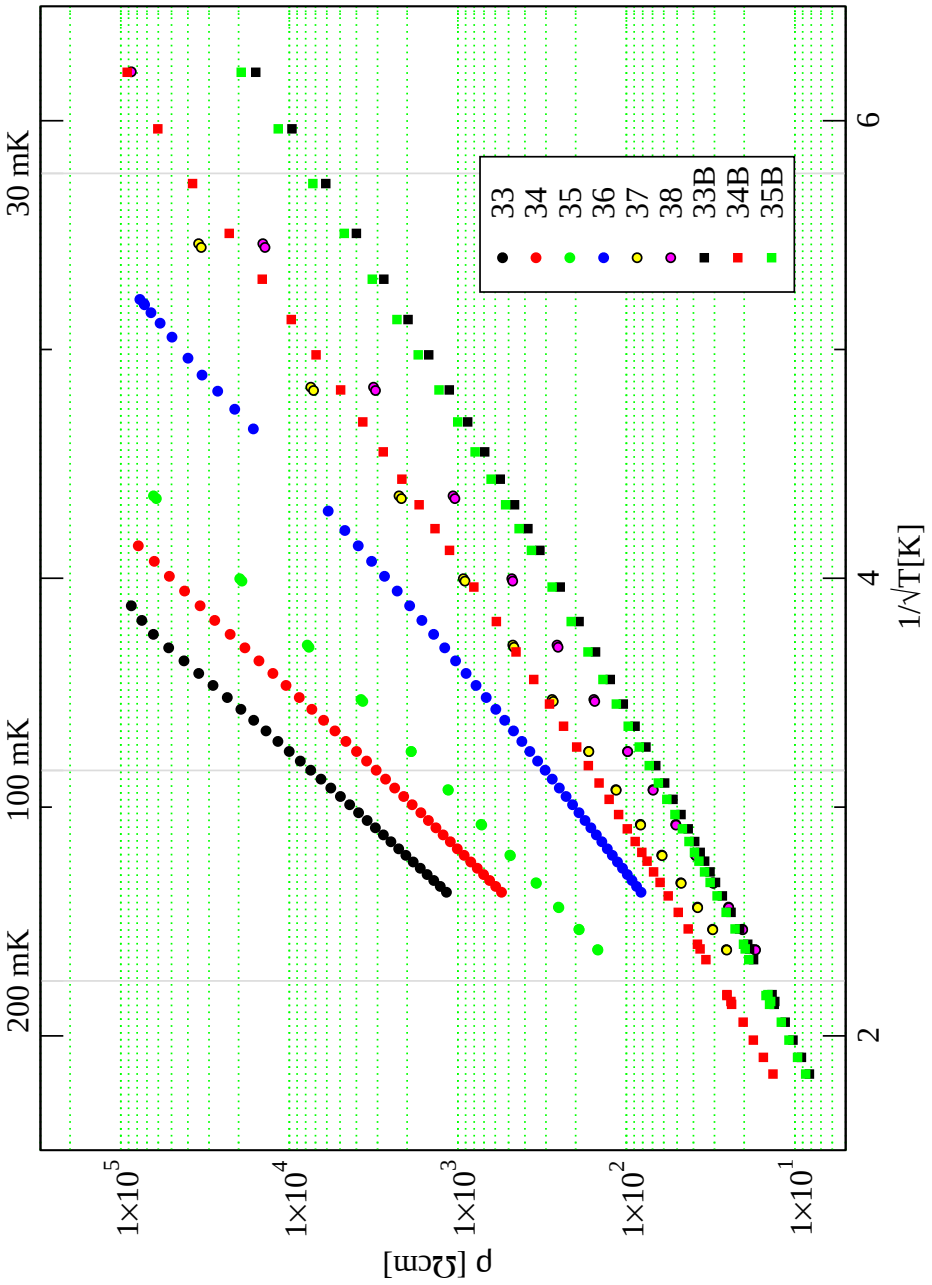

Figure 4.3: Resistivity of all the NTD samples produced for the CUORE project as a funtion of the temperature.

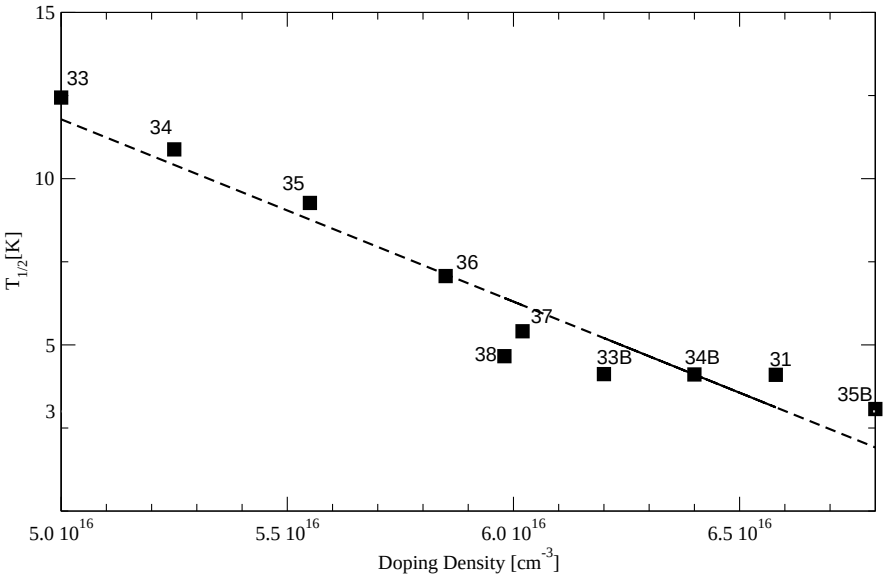

Figure 4.4: $T_{1/2}$ parameter as a function of doping density for the various NTD produced for CUORE. The parameter is found to decrease with the increase of doping density, as expected.

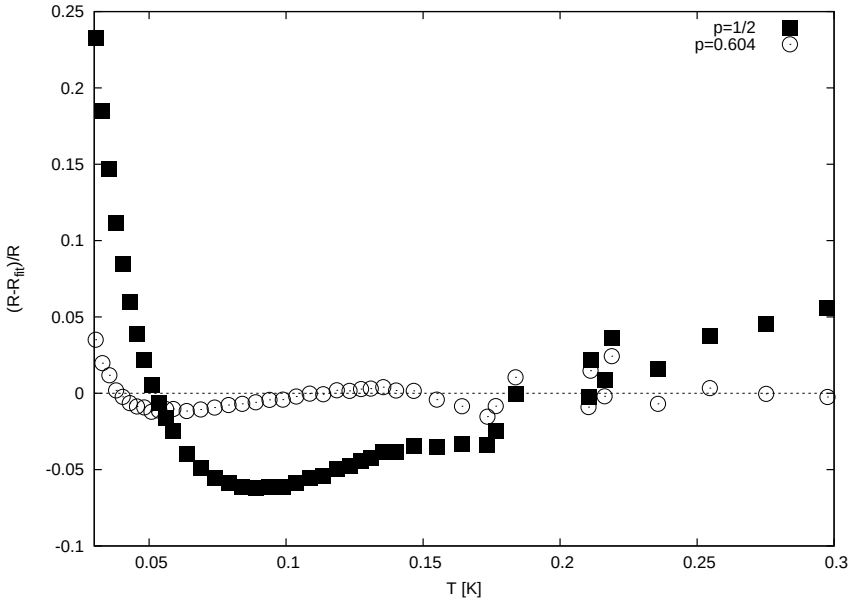

Figure 4.5: Deviation of the fit of the generalized Mott law Equation (2.13) from the experimental points. Square points are fit with a fixed $p = 1/2$. Circle points are fit with varying p. $T_{1/2}$ is found to be inversely proportional to the doping density, Figure (4.4).

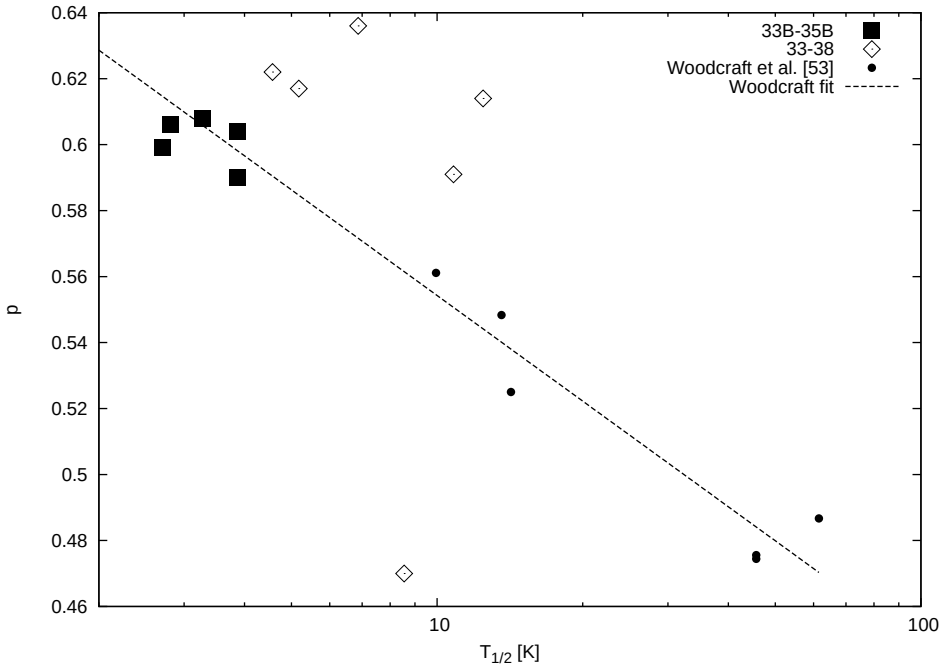

Figure 4.6: The parameter p as a function of $T_{1/2}$; square points are NTD type 33B (two samples), 34B, 35B (two samples) diamond points are NTD type 33, 34, 35, 36, 37, 38, circle points are from [53]. $T_{1/2}$ is found to be inversely proportional to doping density, Figure (4.4).

vary. Moreover they find that the p parameter is proportional to the doping density. In Figure (4.6) we show a merge of Woodcraft et al. data with measurements of the produced NTD thermistors.

We can see that NTD samples of type 33B (two samples), 34B, 35B (two samples), fit reasonably well with Woodcraft data and extrapolation, while the thermistor of type 33 to 38 lie quite far from the fit. A possible explanation is that the data of the latter samples refer to datasets with not enough datapoints and to a too small range of temperature (70-140 mK), which gives disperse results.

The merge gives an enhancement of Woodcraft data enabling us to investigate a "quite" large spread of doping density: ranging from a $T_{1/2}$ of about 3 K to more than 60 K.

NTD Type	Dimensions [mm^3]	$T_{1/2}$ [K]	$R_{1/2}$ [Ω]	Doping [52] [cm^{-3}]	p
33	2.9x1.6x6	12.44 ± 0.08	0.328 ± 0.001	5.0 10^{16}	0.61 ± 0.01
34	2.9x1.6x6	10.88 ± 0.05	0.278 ± 0.001	5.3 10^{16}	0.59 ± 0.05
35	2.9x1.6x6	9.27 ± 0.08	0.342 ± 0.001	5.6 10^{16}	0.47 ± 0.01
36	2.9x1.6x6	7.07 ± 0.05	0.208 ± 0.001	5.9 10^{16}	0.636 ± 0.001
37	2.9x1.6x6	5.41 ± 0.07	0.281 ± 0.001	6.0 10^{16}	0.617 ± 0.002
38	2.9x1.6x6	4.66 ± 0.06	0.283 ± 0.001	6.0 10^{16}	0.622 ± 0.002
33B_1	3x3x1	3.86 ± 0.04	0.830 ± 0.001	6.2 10^{16}	0.599 ± 0.001
33B_2	3x3x1	2.84 ± 0.04	0.830 ± 0.001	6.2 10^{16}	0.599 ± 0.001
34B	3x3x1	3.87 ± 0.04	0.835 ± 0.001	6.4 10^{16}	0.590 ± 0.001
35B_1	3x3x1	2.92 ± 0.03	0.949 ± 0.001	6.8 10^{16}	0.596 ± 0.001
35B_2	3x3x1	3.27 ± 0.03	0.949 ± 0.001	6.8 10^{16}	0.596 ± 0.001

Table 4.2: Data of the 9 NTD series produced for CUORE, and of NTD 31; doping is the compensate doping: #Ga-#As-2#Se.

Conclusions

Measurements of ultra-low temperature electrical conductivity of several kinds of NTD Germanium samples have been investigated. NTD samples have been produced in the frame of the CUORE experiment.

The equation Equation (2.13)

$$R(T) = R_p \exp\left(\frac{T_p}{T}\right)^p$$

is very good function to fit all the data. However the agreement of datapoints with the classical Coulomb Gap theory of VRH seems not to be satisfactory. As a matter of fact, significant systematic deviation from the experimental data points can be found when fitting with a $p = 1/2$, as shown in Figure (4.5).

On the other hand, fitting Equation (2.13) leaving p as a parameter, enhances the accuracy of the fit, and the resulting p is in correlation with the doping density: see [53] and Figure (4.6).

Moreover Woodcraft et al. [53], state that the variation of p is intrinsic of the sample, excluding possible "crossover" between two different values of p as

the temperature is changed. Our results, are in agreement with Woodcraft interpretation, and give a substantial enlargement of the analyzed doping density range.

Chapter 5

Non Linearities

In this chapter we will investigate the ultra low temperatures non linearities cited in §(2.2). During this work many NTD samples have been measured, §(4.2); part of those have been furtherly investigated to find the electron-phonon decoupling parameters: the chosen samples are NTD 36, 38, 34B. The selected samples cover a "wide" range of doping density.

5.1 Experimental Method

Data analysis and acquisition methods are deeply correlated. We describe data analysis method in §(5.1.1) and the experimental details in §(5.1.2).

5.1.1 Data Analysis

The Hot Electron Model, Figure (5.1), can be used to fit experimental data. Let us resume the main characteristics and assumptions of this model; a more detailed description is given in §(2.2).

1. a NTD sample can be described by two different subsystems, electrons (charge carriers) and phonons;

2. the charge carriers (either electron or hole) are at thermodynamic equi-

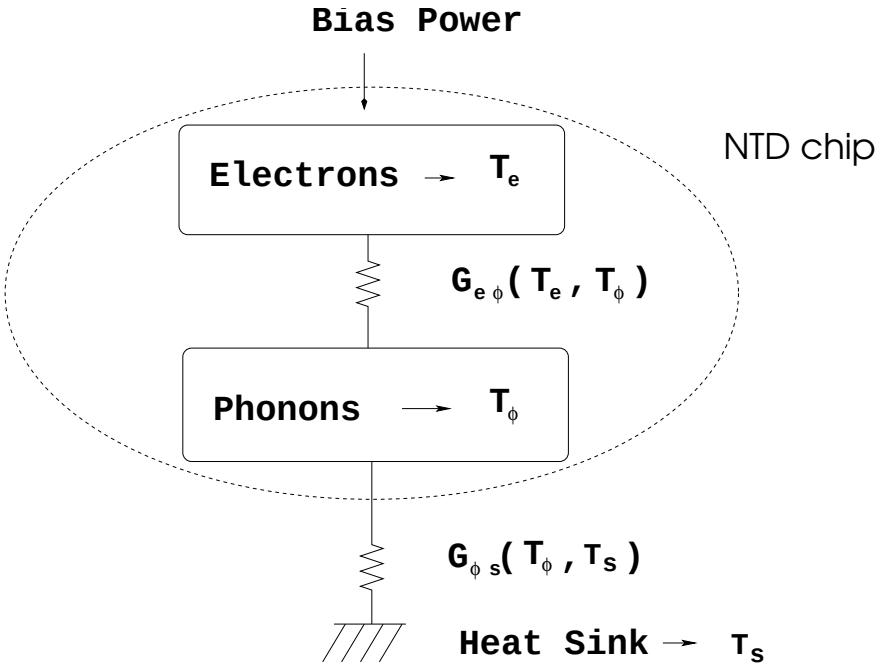

Figure 5.1: Schematic of Hot Electron model

librium, hence a temperature, T_e, of the subsystem can be defined;

3. the phonon subsystem, as well, is at thermodynamic equilibrium and a temperature T_ϕ can be defined;

4. the T_e can be measured by means of Equation (2.13):

$$\rho = \rho_p \exp\left(\frac{T_p}{T_e}\right)^p$$

5. the bias power is totally deposited in the electron subsystem;

6. the thermal conductivity between electrons and phonons, $k_{e\phi}(T)$ has a power law temperature dependence, Equation (2.26):

$$k_{e\phi}(T) = (\beta + 1)\ g_{e\phi}\ T^\beta \quad [\mathrm{W/K^2}] \tag{5.1}$$

where β and $g_{e\phi}$ are constants that do not depend on temperature.

The NTD sample is thermally connected to the heat sink by another thermal conductance, from the sample to the sink, originated by contact between sample and holder surfaces (Kapitza conductance).

The Kapitza thermal conductance links the phonon subsystem to the sample holder,

$$G_K(T_\phi, T_b) = \frac{1}{T_\phi - T_b} \int_{T_b}^{T_\phi} k_{\phi b}(T) dT \tag{5.2}$$

where $k_{\phi b}(T)$ is the thermal conductivity from the sample to the sink, and it is expected to be proportional to T^α (with $\alpha \approx 3$):

$$k_{\phi b}(T) = (\alpha + 1) g_{\phi b} T^\alpha \tag{5.3}$$

where α and $g_{\phi b}$ are the two constant parameters.

Referring to Figure (5.1), a power P, impinging into the sample, flows through both the thermal conductances $G_{e\phi}$ and $G_{\phi b}$:

$$P = G_{e\phi}(T_e, T_\phi)(T_e - T_\phi) = g_{e\phi} \left(T_e^{\beta+1} - T_\phi^{\beta+1} \right) \tag{5.4}$$

$$P = G_{\phi b}(T_\phi, T_b)(T_\phi - T_b) = g_{\phi b} \left(T_\phi^{\alpha+1} - T_b^{\alpha+1} \right) \tag{5.5}$$

The power P heating the sample is the sum of two different contributions: the power P_m supplied during the measurement and the spurious power, P_s, coming from EM-radiation and from cryostat vibrations.

$$P = P_m + P_s \tag{5.6}$$

Imposing a measurement power, P_m, we define a temperature gradient in the NTD sample subsystems; hence, to each P_m correspond a couple of equations 5.4 and 5.5 with respective T_e and T_ϕ.

On the other hand, while P_m, T_e and T_b can be measured, we have no access to T_ϕ, since the phonon subsystem it is a purely theoretical concept. Therefore, the measurement of the electron-phonon decoupling is not straightforward as might be the measurement of the thermal conductivity of a material; here we cannot directly measure the temperatures at the ends of the sample (we do not have a sample either).

Summarizing:

- we will refer to a measure as to the triplet (P_m, T_e, T_b);
- a temperature gradient in the sample $(T_e(P_m), T_\phi(P_m))$ and the couple of Equation (5.4) and Equation (5.5) corresponds to each measure.
- the unknown parameters in Equation (5.4) and Equation (5.5) are the electron-phonon decoupling parameters β and $g_{e\phi}$, the Kapitza decoupling parameters α and $g_{\phi b}$, the temperature of the phonon subsystem T_ϕ and the spurious power P_s.
- all unknown parameters (except T_ϕ) are constant through all the measures.

We have acquired N measures in a wide range of biasing power: P_m ranging from 10^{-15} to 10^{-9} W. Numerical solutions of the resulting set of N Equation (5.4) and Equation (5.5) are found by means of MINUIT package (CERN) using non linear fitting algorithm. The initial guess to provide to the algorithm is found as explained below.

We expect the Kapitza thermal conductivity to be much more relevant than electron-phonon conductivity in "high" temperature range (above 40–50 mK). In this temperature range we suppose electron-phonon thermal conductivity to be infinite so that $T_e \equiv T_\phi$. Hence, from "high" temperature range measurments we can determine, by means of Equation (5.5), the parameters of the $k_{\phi b}(T)$ Kapitza thermal conductivity: α and $g_{\phi b}$.

In the "low" temperature range (below 30 mK) we expect the two thermal conductivity to be of the same order of magnitude; we use the previously derived Kapitza thermal conductivity parameters, to determine the N T_ϕ.

5.1.2 Experimental set-up

NTD samples are glued on the copper holder as described in §(4.2). In Figure (5.2) the thermal model of NTD chip and wires connection is sketched. The bias power P_m has two ways to flow to the heat sink: through the NTD chip and through the electrical connections.

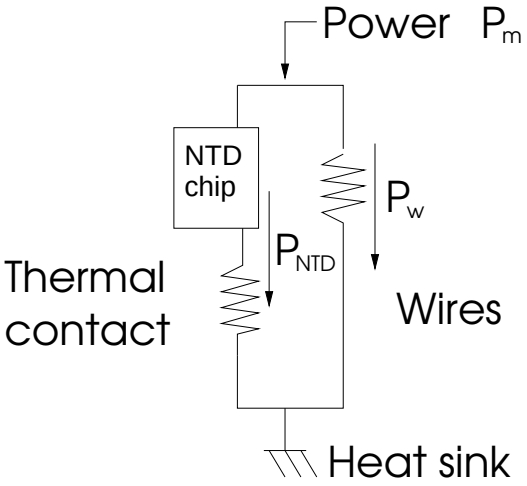

Figure 5.2: Schema of the thermal model of the wires effect.

In order to minimize the power flowing via the electrical connections, the gold wires are soldered to Al tubes: as a matter of fact, aluminium is a superconductor ($T_c = 1.1$ K) and therefore it is bad thermal conductor. In this way the thermal conductance to the bath given by the wires tends to be infinite, hence $P_w \to 0$. To solder the gold wire (50 μm diameter) to the aluminium tube (100 μm inner diameter, 200 μm outer diameter), we plug the wire into the tube, and then we crimp the tube. Since the thermal contraction of Al is larger than that of Au, the lowering of the temperature helps to keep the link well tight.

A calibrated RuO_2 thermistor is used to measure the heat sink temperature, and a copper thermal shield at the base temperature surrounds the sample holder.

As described in §(5.1.1) a number N of measures (triplet P_m, T_ϕ, T_b) are needed to extrapolate the electron-phonon decoupling parameters. Measures are acquired by setting a heat sink temperature, T_b, and then by making current-voltage curves (load curves) with a increasing bias current I. In this way we dissipate on the NTD sample, a power $P_m = VI$, by Joule effect.

We have acquired a number of load curves for each NTD sample in a temperature range of about 20–60 mK. The typical dissipated power P_m is ranging from 10^{-15} to 10^{-9} W. An example of load curves for a sample at

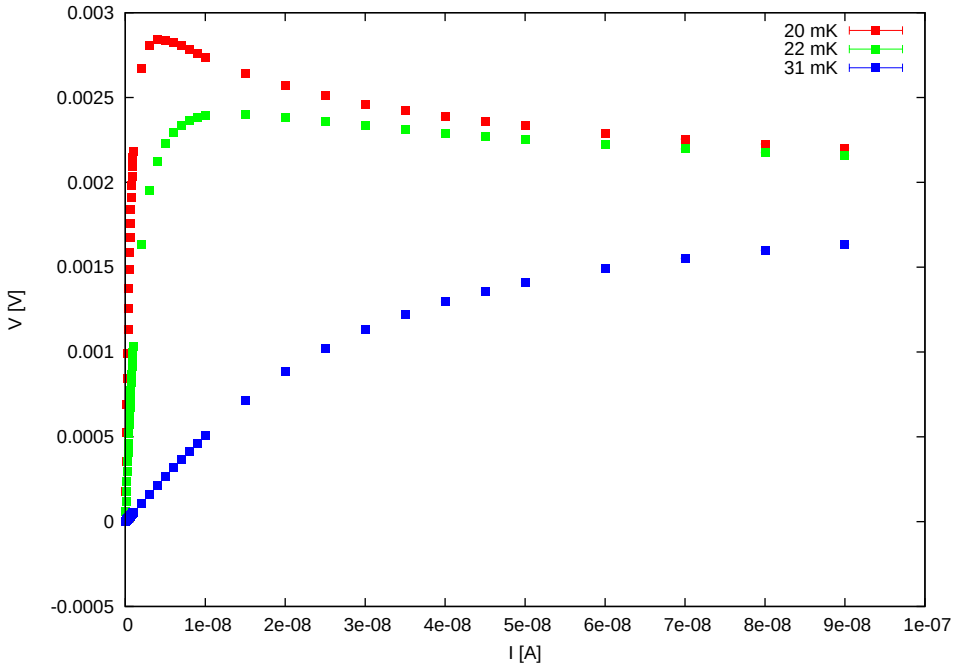

Figure 5.3: Example of load curves for one NTD sample, at different base temperature.

various heat sink temperature is shown in Figure (5.3).

Instrumentation

DC measurements on the NTD samples are done by means of a Keythley 236 current generator (capable to circulate currents from 10^{-15} A to 1 mA) and a Keythely model 2000 multimeter. An AVS-47 resistance bridge is used to measure the temperature of the heat sink, and a AFG-200 function generator is used to set the base temperature.

Data acquisition is automatically run by a computer that communicates with the instruments via GPIB bus[1].

The current to bias the NTD chip is set and a large number (150) of

[1]The computer is a Pentium-S 100 MHz and runs Debian GNU/Linux 3.0r3 (kernel 2.4.18); the GPIB card is a IOTech 488 with a NEC 7210 chip. The module driver is linux-gpib: the module sources can be found at `http://linux-gpib.sourceforge.net`, and can be downloaded with GPL licence.

voltage measurement are acquired. After this step, the inverse current is set and the same number of voltage measurements is performed.

During analysis, as a first step, average and standard deviation of 150 voltage measurements are calculated in order to reduce errors in data. Since the measured voltage across the sample, ΔV, is influenced by a parasitic voltage, V_0, across the sample

$$\Delta V = V_m + V_0$$

where , V_m is the voltage due to the flowing current. Hence, V_m across the chip is obtained, as a second step, by two measurements with $+I$ and $-I$ as

$$V_m = \frac{\Delta V^+ - \Delta V^-}{2}$$

since the parasitic voltage depends on the flowing current.

5.2 Results and Discussion

In table Table(5.1) we report the results of the fit of electron-phonon decoupling parameters as described in §(5.1.1). In Figure (5.4), Figure (5.5) and Figure (5.6) we show the fit of experimental data for NTD 36, NTD 38 and NTD 34B respectively.

In Table(5.2) we have collected the values of the Hot Electron Model for NTD Germanium present in literature. The comparison of our results with these values is not easily done:

- not all the authors actually fit the experimental data, but some [37, 54] fix the value of β to 4 and 5, respectively.

- three authors report measurements of electron-phonon decoupling on the same type 23 NTD, [37, 54, 55]; we note that the $T_{1/2}$ value is completely different in the 3 references, ranging from 2.2 to 3.93 K. The same effect is reported by [37] for NTD type 12 that has different $T_{1/2}$ ranging from 6.8 to 7.7 K.

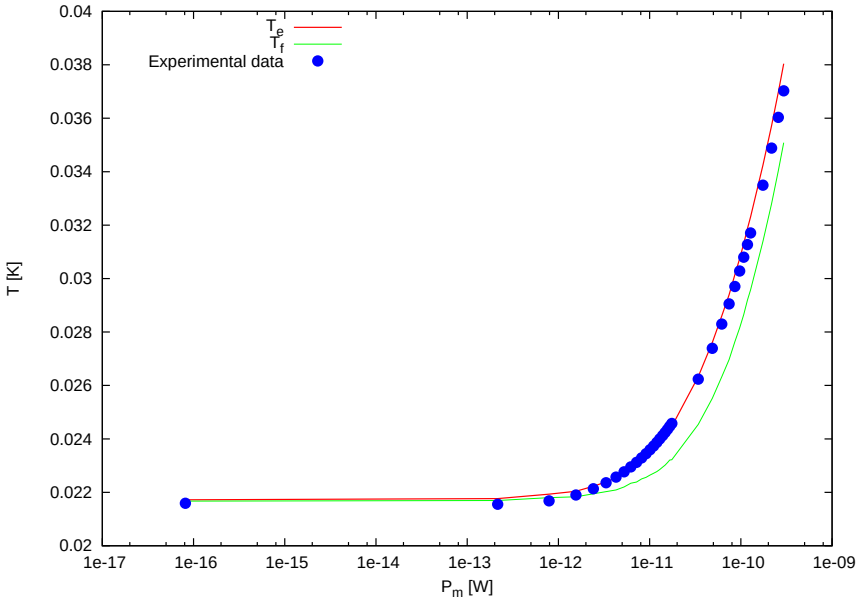

Figure 5.4: Electron-phonon decoupling effect in NTD 36. Green line is the phonon temperature, red line is the electron temperature as extracted by means of the electron-phonon decoupling parameters.

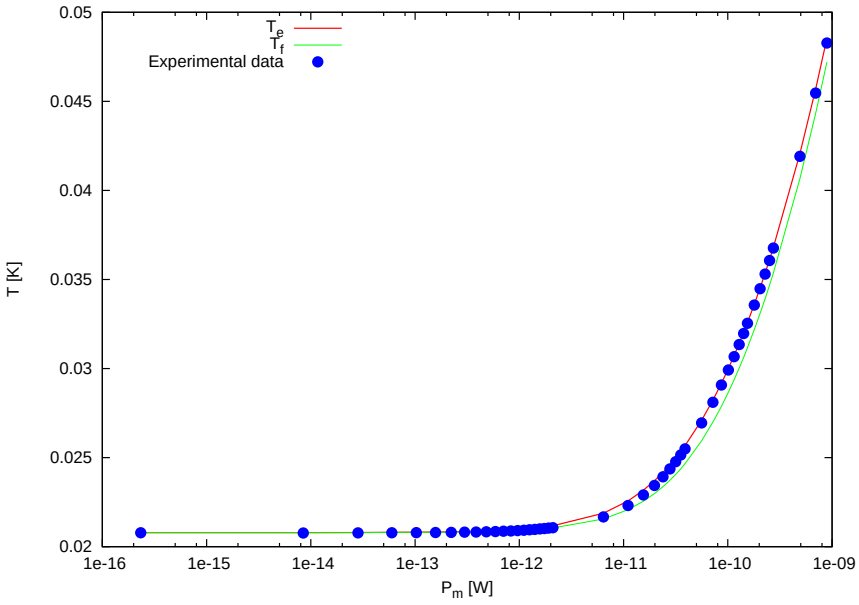

Figure 5.5: Electron-phonon decoupling effect in NTD 38. Green line is the phonon temperature, red line is the electron temperature as extracted by means of the electron-phonon decoupling parameters.

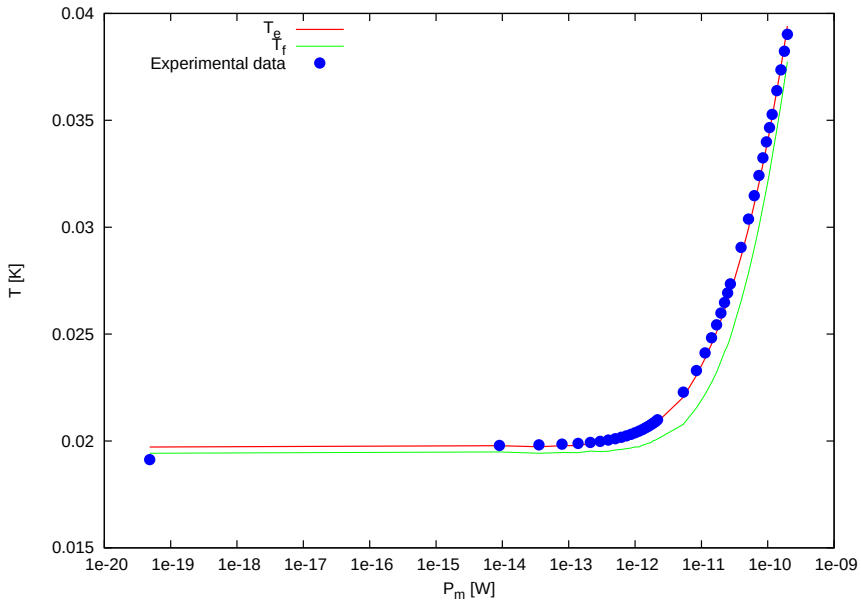

Figure 5.6: Electron-phonon decoupling effect in NTD 34B. Green line is the phonon temperature, red line is the electron temperature as extracted by means of the electron-phonon decoupling parameters.

Anyway, a possible comparison of the various measurements can be done by looking at the values of the conductivity per unit volume at a certain temperature T

$$k_{e\phi}(T) = \frac{(\beta+1)g_{e\phi}T^{\beta}}{V}$$

In the last column of Table(5.2) we report the value of the conductivity per unit volume at 30 mK; $k_{e\phi}(30\text{ mK})$, for all the references, groups in less than one order of magnitude, if we discard the result of [55]. This indicates a substantial agreement of the data, even if the measurements are still "quite" disperse.

As a matter of fact, all the measurements reported in Table(5.2) refer to data above 20 mK. The electron-phonon decoupling should be more relevant as the temperature is lowered, hence temperature measurement at lower temperature should be done. In our case the limitation in the lowest temperature was given by the dilution refrigerator whose minimum temperature is about 20 mK.

NTD type	36	38	34B
α	2.76	2.75	2.74
$\Delta\alpha$	0.02	0.04	0.06
$g_{\phi b}$ [W K$^{-(\alpha+1)}$]	1.04E-04	8.658E-05	4.610E-05
$\Delta g_{\phi b}$	5.80E-06	1.290E-05	6.500E-06
β	4.53	4.44	5.43
$\Delta\beta$	0.18	0.44	8.00E-002
$g_{e\phi}$ [W K$^{-(\beta+1)}$]	5.799E-02	8.728E-02	8.80E-001
$\Delta g_{e\phi}$	4.400E-03	1.323E-02	1.700E-01
l [mm]	2.900E+00	2.900E+00	3.000E+00
S [mm^2]	1.140E+01	1.140E+01	3.000E+00

Table 5.1: The results of the electron-phonon decoupling parameters as found by analysis described in §(5.1.1)

Reference	NTD type	$T_{1/2}$ [K]	β	$g_{e\phi}$ [W K$^{-(\beta+1)}$]	$k_{e\phi}$(30mK) [W K^{-1}mm^{-3}]
Soudée [37]	23	3.2	**4**	2.4 10^{-3}	4.6 10^{-9}
Wang [35]	12	6.8–7.7	5	8.0 10^{-3}	5.8 10^{-9}
Aubourg [54]	23	3.93	**5**	9 10^{-2}	8.7 10^{-9}
Alessandrello [55]	23	2.2	4.6	7 10^{-1}	6.5 10^{-8}
Pasca [39]	31	3.5	4.5	7 10^{-2}	1.9 10^{-9}
This work	34B	4.14	5.4	8.8 10^{-1}	3.4 10^{-9}
This work	38	4.66	4.4	8.7 10^{-2}	2.5 10^{-9}
This work	36	7.07	4.5	5.8 10^{-2}	1.23 10^{-9}

Table 5.2: Experimental values of Hot Electron model present in literature in comparison with the data obtained in this work. The bold face β refer to values fixed by authors. On the last column we report the electron-phonon thermal conductivity per unit volume $k_{e\phi}(T) = (\beta+1)g_{e\phi}/VT^{\beta}$, calculated at 30 mK, to compare the results.

Chapter 6

Transport Properties in Magnetic Field

We have studied the behaviour of 3 samples of NTD Germanium type 25, and of one type 35B, in the ultra low temperature and high magnetic field range. The investigated magnetic field range was 0–5 T and the temperature range was 65–200 mK.

As seen in §(4.2), type 25 and type 35B are among the most doped samples produced. For a rough comparison $T_{\frac{1}{2}}(25) \approx 1.25$ K and $T_{\frac{1}{2}}(35\text{B}) \approx 3$K.

The sample geometry is 2x2x1 mm^3 for the type-25 samples and 3x3x1 mm^3 for the NTD 35B sample. In particular, the ion implanted surfaces are the two opposite 2x1 or 3x1 mm^2. The thickness of the sample is always 1 mm.

6.1 Experimental Setup

The dilution refrigerator used for these measurements was equipped with a superconducting coil able to produce a maximum field intensity of 5 T on the sample holder, while the field intensity was highly reduced above the solenoid by means of a compensation coil.

Moreover, to reduce the effect of eddy currents on the refrigerator, the

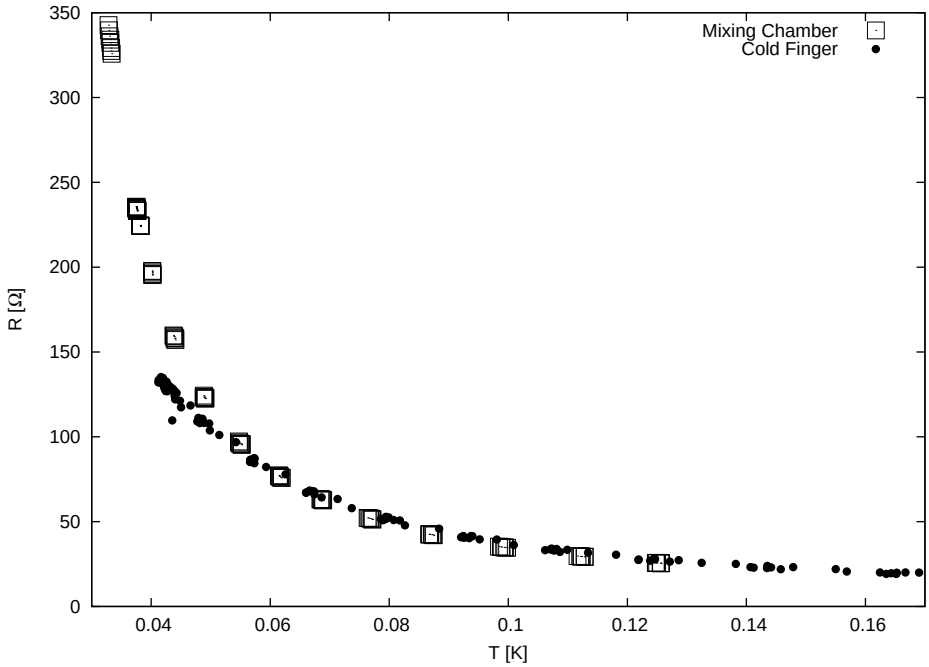

Figure 6.1: Zero field calibration of NTD 25B. Square points: Firenze refrigerator; Cirlce points: Leiden refrigerator.

sample holder was put in the middle of the superconducting coil by means of a 30 cm long copper cold finger, keeping the refrigerator far from the strong field region.

The thermometer that we have used is a calibrated rutenium oxide resitor; it is put in contact with the mixing chamber of the refrigerator, instead than next to the NTD Germanium samples, since the rutenium oxide thermistors show magnetoresistance [56].

At every temperature, residual field on the mixing chamber (caused either by the magnet itself or by magnetization of the steel of the IVC, when the magnet is off) can lead to a resistance of the thermometer completely different to the zero field one. Moreover the eventual presence of eddy current either on the sample holder or on the cold finger can heat up the holder with respect to the mixing chamber.

Both effects cause a wrong measurement of the temperature of the sample holder. Therefore we performend two calibrations, of the Ge samples, in zero

Sample	Orientation
25B	Charge carrier velocity orthogonal to magnetic field direction; charge carrier moved towards small sides of chip (2x1 mm^2).
25C	As 25B but charge carriers moved towards large faces (2x2 mm^2).
25D	Charge carriers velocity parallel to magnetic field.
35B	As 25C

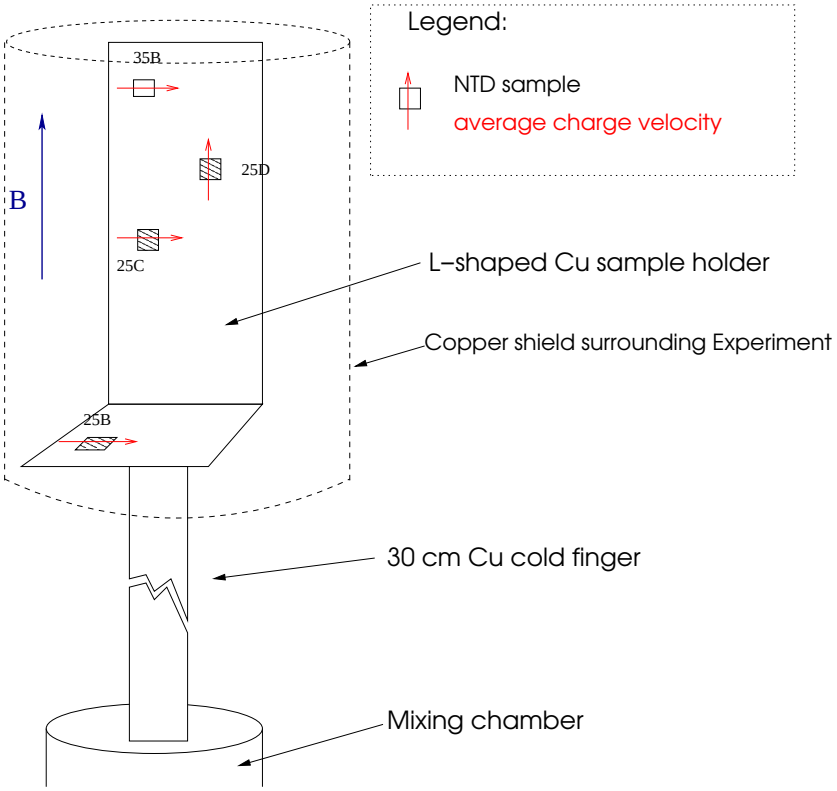

Figure 6.2: Schematic of the experimental setup. The direction of the magnetic field is indicated.

field, with respect to the same calibrated rutenium oxide resistor: one on the refrigerator equipped with the magnet coil [1] and one on a different refrigerator that has never been put in a magnetic field [2]. We checked the overlap of the two different calibrations.

The result, shown in Figure (6.1), is that for temperatures below 65 mK, with any magnetic field, the temperature measurement is not reliable. For this reason we discard measurements below 65 mK.

The 4 samples are mounted with different orientation with respect to the magnetic field in order to see a field orientation dependance of the magnetoresistivity, Figure (6.2).

The samples are mounted as described in §(4.2). Resistance measurements are done with a four probe method: the electrical connections on two opposite surfaces (2x1 or 3x1 mm^2) were made with ultrasonically ball-bonded 50 micron-diameter Au wire. Since four wire resistance measurements were performed, two manganin 100 micron diameter wires were soldered to each Au wire. Filters were used to prevent RF pick up.

Resistance mesurements, at various magnetic field and temperature, are made by loading a fixed current in the superconducting coil, and by changing the temperature of the samples, in constant magnetic field. Resistances of the samples, at each temperature, are acquired by means of an AVS-47 AC resistance bridge. After a complete sweep of the temperature range, we changed the current in the magnet (and hence the magnetic field), and performed a new temperature sweep.

In Figure (6.3) we report the temperature dependance of the resistivity of the 4 samples. Colors of the datapoints are relative to different magnetic field intensity: yellow is 0 T, red is 1 T , green is 2 T, blue is 3 T , magenta is 4 T and cyan is 5 T. A clear effect of magnetoresistance is visible.

[1] Measurements in Magnetic field have been carried out in the Kamerlingh-Onnes Laboratory, Leiden University, The Netherlands.

[2] In our laboratory in Firenze

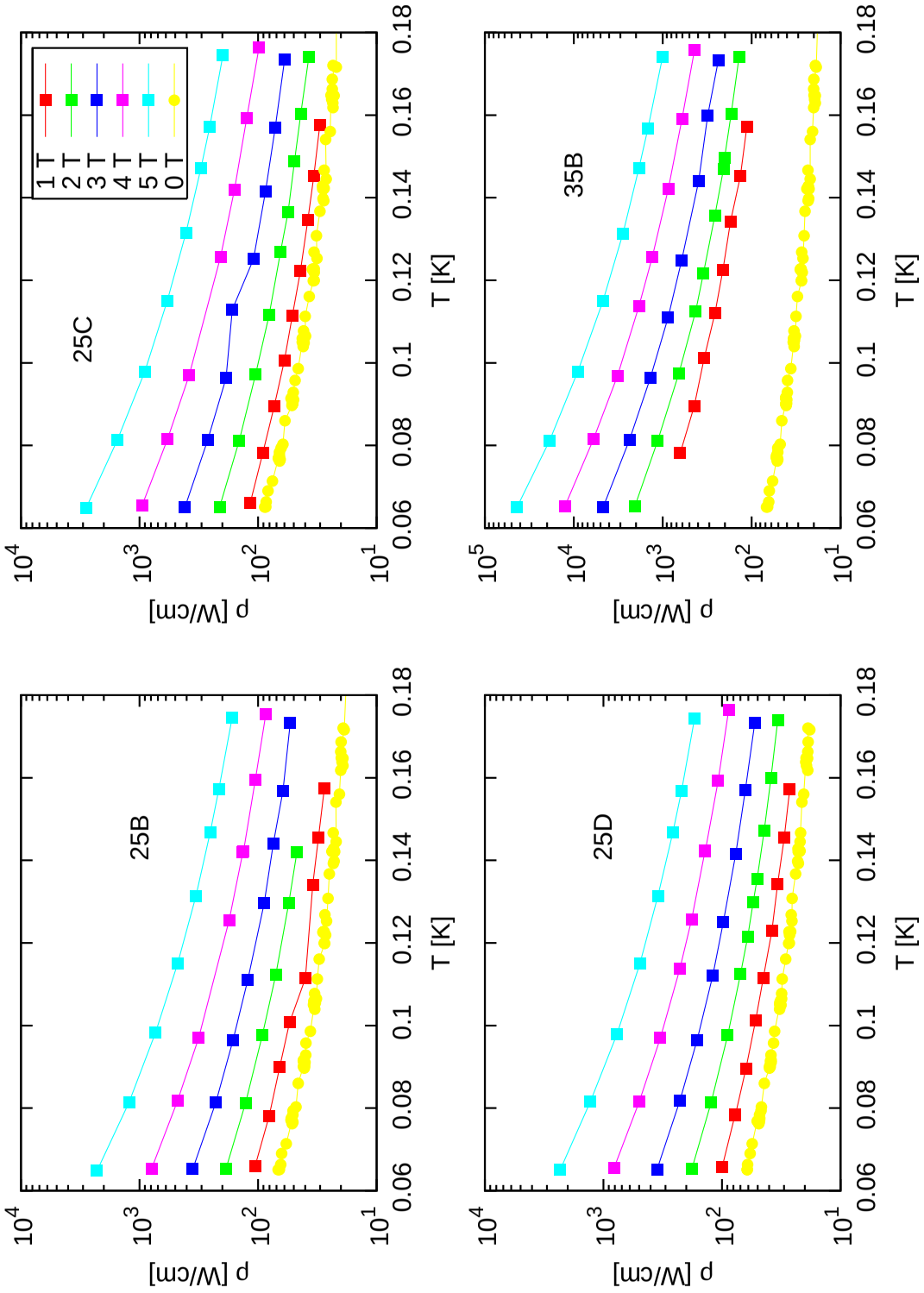

Figure 6.3: Resistance as a function of temperature for the 4 NTD Ge samples.

6.2 Results and Discussion

6.2.1 VRH in Magnetic Field

First of all we performed a fit of a generalized Mott law (Equation (2.13)), letting the parameter p to vary. The method used is a minimum least square fit on a linearized Mott law, i.e.

$$(1/T)^p = a + b\log(R[\Omega]/1\Omega)$$

The best fit is the one with the minimum of χ^2, of the previous equation.

The parameter p

In Figure (6.4) we can see the behaviour of the p parameter with respect to the magnetic field intensity. The zero field parameter is about 0.5 for all the four samples, as expected for a Variable Range Hopping mechanism where a Coulomb Gap plays an important role. We immediately notice that the three 25 type NTD chips give a zero field p value that is ranging from 0.45 to 0.4, while the estimation of the parameter itself is given with much less error. Hence the same material does have different p values. This can be partially explained by the different strains of the samples when they are glued on the sample holder. Unfortunately, independently on how much care is used when glueing the samples, the process is not fully reproducible.

When the magnetic field is switched on, we see from Figure (6.4), that the p parameter tends to decrease. We notice a different behaviour with respect to the orientation of the sample on the magnetic field. In particular for the samples 25B, 25C and 35B, the motion of the charge carriers is orthogonal to the magnetic field lines. For these 3 samples the p parameter shows a crossover from the CG regime in no magnetic filed, with $p \approx 1/2$ to a regime in which $p \approx 1/3$.

As seen in §(2.3), we would expect, for a VRH where a Coulomb Gap plays a fundamental role, as in these NTD samples, that the p parameter would increase from about 1/2 to 3/5. Instead, in this case we observe a

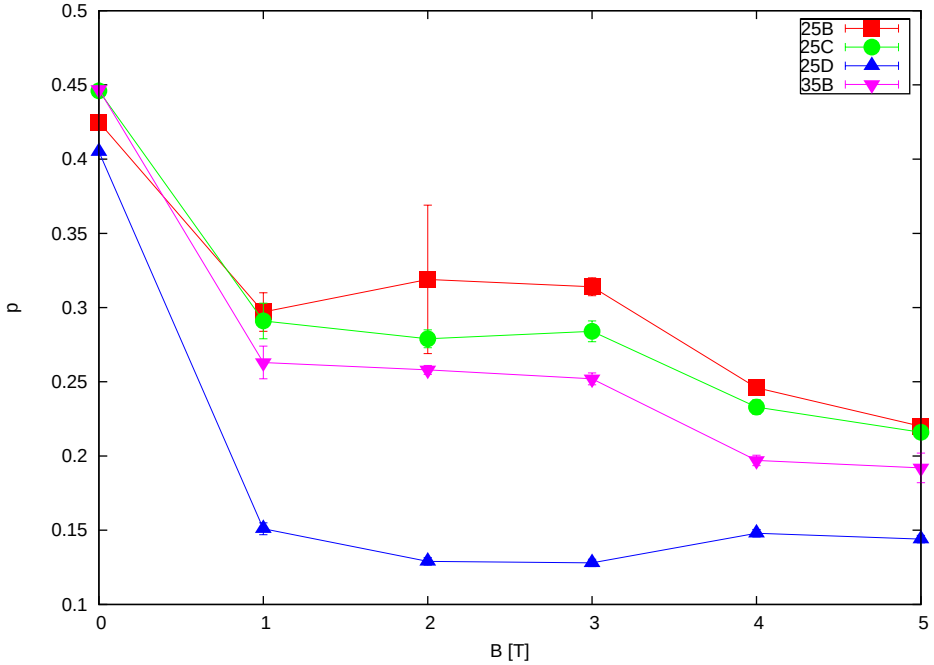

Figure 6.4: Behaviour of the parameter p of the Equation (2.13), as a function of magnetic field for the 4 NTD Ge samples.

decrease of p from 1/2 to about 1/3, within 4 T; such a behaviour has been reported by other authors [47, 46].

We give here a possible explanation to this behaviour: the Coulomb Gap is effective only at sufficiently low temperatures, $k_bT < \epsilon_{CG}$, where ϵ_{CG} is the energy at which the density of states at the Fermi level returns to its unperturbed (constant) value. As we have seen in §(2.1.2), in the Variable Range Hopping conduction mechanism the caracteristic hopping lenght, λ increases as temperature decreases. In other words, if the CG is effective, $\lambda(T)$, must be bigger than a critical lenght λ_{CG}.

$$\lambda(T) > \lambda_{CG}$$

When a magnetic field is superimposed to the sample, the field tends to decrease the overlap between wave function of charge carriers (the wave functions are stretched), and therefore the hopping lenght is reduced; in this way λ can decrease to values lower than the critical λ_{CG}, making the Coulomb Gap to be less effective [47].

The increase of the magnetic field leads to a further decrease of the p parameter. In this case, the model that has been used in §(2.1) and §(2.3) does not hold anymore because it leads to a divergence of the density of states at the Fermi level. As a matter of fact, the parameter m of Equation (2.12), for $p < 1/3$ becomes negative (in the case described in §(2.3.1), while in the case of Coulomb Gap theory $m < 0$ for $p < 1/4$). Nevertheless, the resistivity can still be fitted with a generalized Mott law.

For what regards the NTD sample 25D, in which the motion of charge carriers is parallel to the magnetic field, we see from Figure (6.4), that the p parameter decreases, because of the influence of the magnetic field, to a value well below 1/3 (about 0.15), with apparently no further field dependance.

$T_{1/3}$ and $R_{1/3}$ parameters

For fields below 4 T, we can fit the $R(T)$ curves of the samples, by a Mott law with $p = 1/3$ and see what is the field dependence of $R_{1/3}$ and $T_{1/3}$ parameters. As discussed in §(2.3.1), we expect $R_{1/3}$ not to show any field dependence, while, from Equation (2.30)

$$T_{1/3} \propto H$$

Unfortunately, we have only 3 datapoint below 4 T, and hence we cannot extrapolate any dependence. The results are shown in Figure (6.5); we can observe that the parameter $T_{1/3}$ is compatible with a linear dependence on the magnetic field, while, no clear field dependence is visible for the parameter $R_{1/3}$.

6.2.2 Magnetoresistance

The main effect of the magnetic field on the NTD samples is the gigantic magnetoresistance which depends exponentially on the magnetic field strenght. We can see the effect, at 100mK for the 4 samples in Figure (6.6).

As discussed in §(2.31), we expect an increase of the resistance following

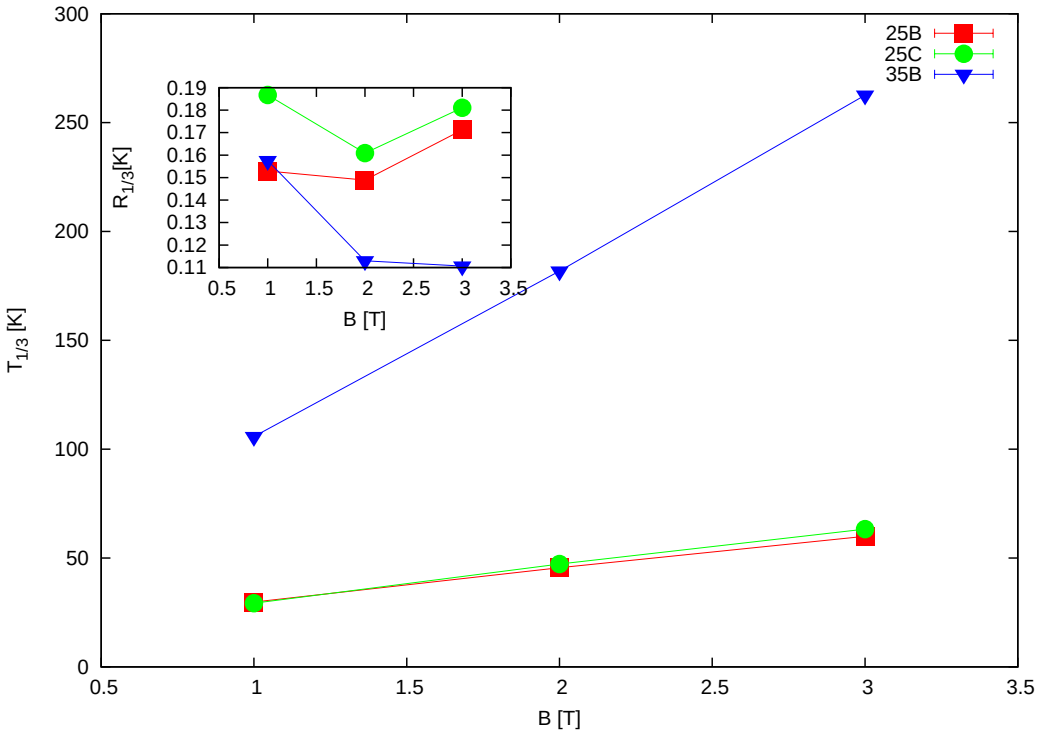

Figure 6.5: The behaviour of the $T_{1/3}$ parameter for the NTD 25B, 25C and 35B as a function of magnetic field. The parameter shows a linear dependence as expected [33]. Anyway, since we can provide only 3 datapoints, we can not investigate further. In the inset the $R_{1/3}[\Omega]$ behaviour as a function of magnetic field is reported.

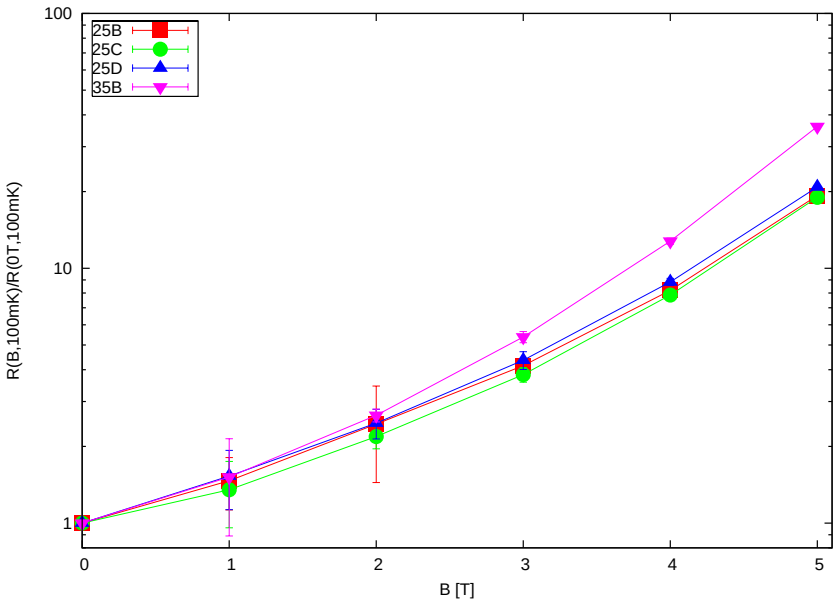

Figure 6.6: Ratio of the resistance in magnetic field and no field resistance of the four NTD samples at 100 mK as a function of magnetic field. Note that the same type Ge show almost the same magnetoresistance.

the exponential law Equation (2.31):

$$\ln F(T,H) = \ln\left(\frac{\rho(T,H)}{\rho(T,H=0)}\right) = \left(\frac{B}{B_0}\right)^{\xi} \tag{6.1}$$

where $\rho(T, H = 0)$ is the zero field resistivity at a temperature T and $\rho(T, H)$ is the resistivity at the same temperature with a not null magnetic field.

We have fitted Equation (6.1) in the 70–150 mK temperature range, and derived the parameters B_0 and ξ. The results are shown in Figure (6.7) and Figure (6.8). From Figure (6.9) we can see that the functional dependence of $F(T, B)$ from the magnetic field is well described by Equation (6.1); we notice that the ξ parameters is almost temperature independent.

On the other hand, the ξ parameter is expected to be dependent on the magnetic field:

- at low fields, ξ is expected to be $\xi = 2$ [46, 33];

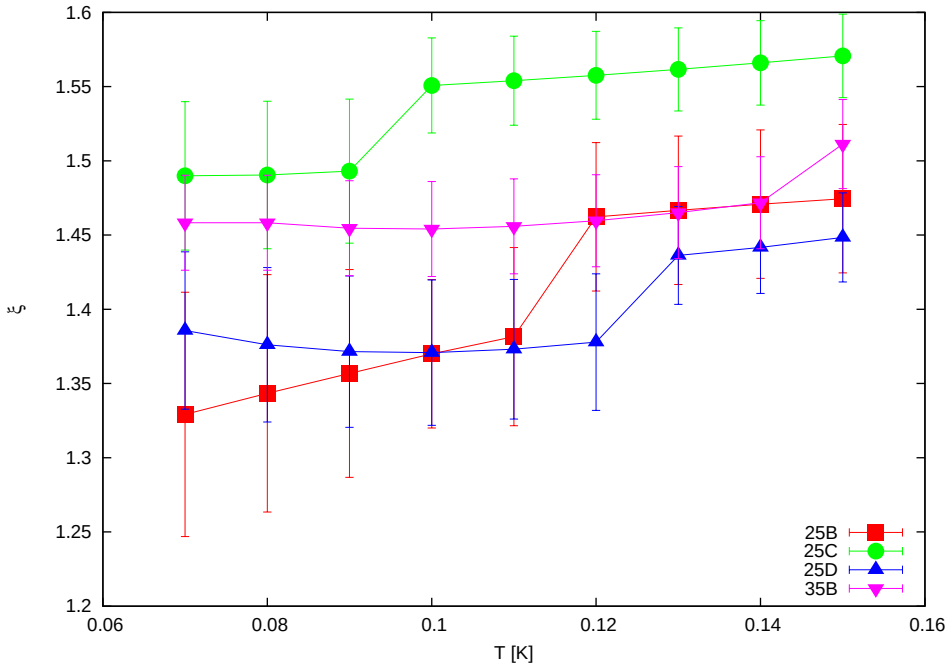

Figure 6.7: ξ value for all the samples at various temperatures.

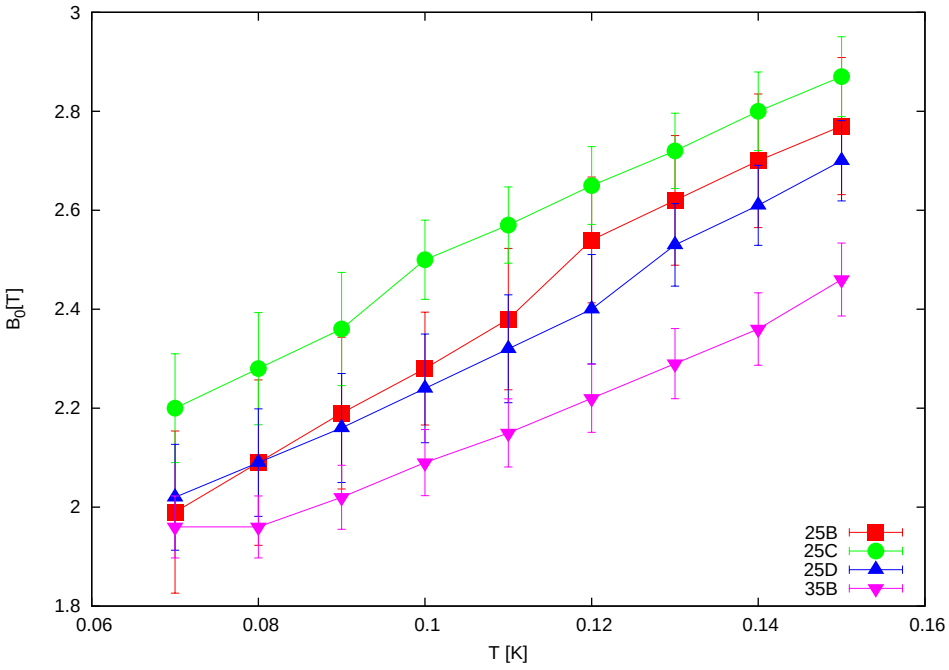

Figure 6.8: B_0 value for all the samples at various temperatures.

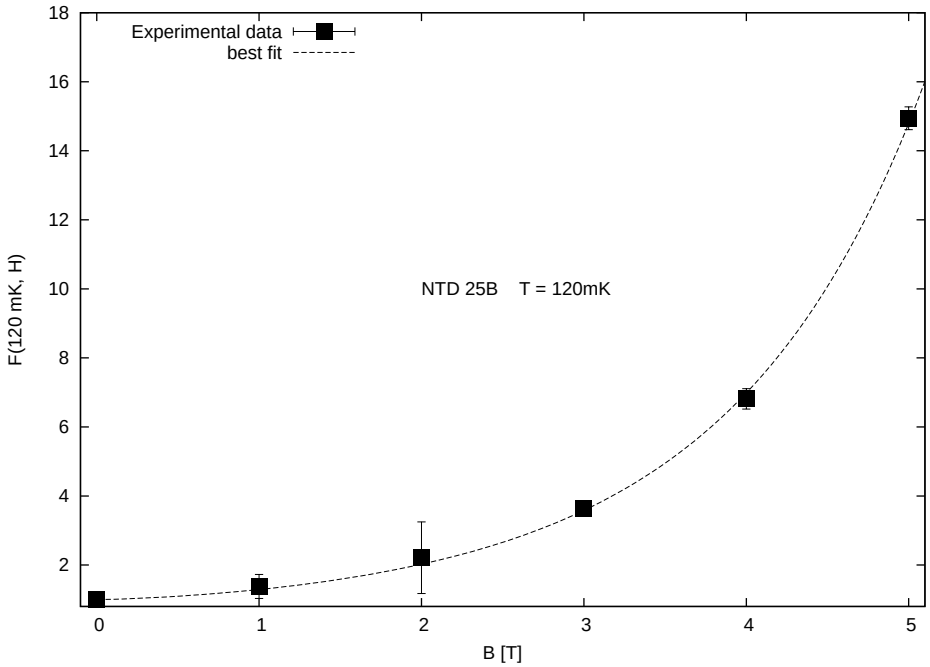

Figure 6.9: Ratio $F(120mK, H)$ for NTD 25B sample, as a function of magnetic field.

- in the high field limit, ξ should ultimately decrease to a value of 1/3 for a constant density of states, or to 1/5 for a Coulomb gap[46].

Nevertheless, authors report experimental values of $\xi \approx 1$, even in high magnetic field [46]. The results obtained here, are coherent with [46]; as a matter of fact, ξ is ranging from 1.3 to 1.6 for all the 4 samples, as shown in Figure (6.7). We should stress that we cannot distinguish between the low field and high field range because data we have collected are too widely separated.

6.2.3 Sensitivity

Since the resistance to temperature dependence is exponential, the NTD thermistors are very sensitive and commonly used as thermometers. The sensitivity is defined as

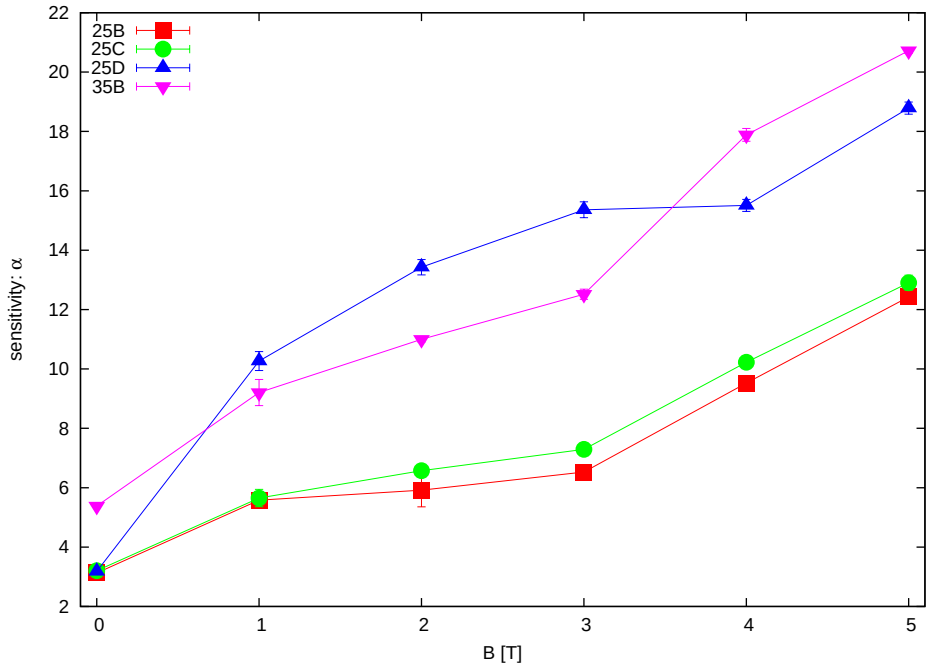

Figure 6.10: Sensitivity of the 4 samples of NTD as a function of magnetic field.

$$\alpha = \frac{d \log R}{d \log T} \tag{6.2}$$

It is interesting to see what is the effect of the magnetic field on the sensitivity of NTD samples, in view of a possible use of them as temperature sensor of bolometers in magnetic field (as might be in the KATRIN experiment[9]). A first effect of the use of the magnetic field can be the possibility to vary the resistance of the sensors by varying the magnetic field on them in order to match the read-out electronic impedance.

Another key effect of the magnetic field on the performances of the NTD samples, is that it tends to increase the sensitivity to temperature variations. As a matter of fact we can see, from Figure (6.10), that the sensitivity of the Ge samples grows, from zero magnetic field to 5 Tesla, of about 400% for the orthogonal samples (i.e. 25B, 25C, 35B) and of about 600% for the NTD 25D (parallel oriented to the magnetic field).

6.3 Conclusions

In conclusion, NTD Germanium in the VRH regime show a gigantic exponential magnetoresistance effect, but the resistance to temperature dependence is still a generalized Mott function, Equation (2.13). The resistance to magnetic field depedence can be fitted by Equation (2.31).

A crossover between the Coulomb Gap VRH mechanism with $p = 1/2$ in the absence of magnetic field to a regime in which $p = 1/3$ in magnetic field is found. In this conditions the minimum of the densisty of states at the Fermi level is no more effective. A further increase of the magnetic field leads to a further decrease of p. The standard gap model, §(2.1.3), does not hold anymore since it leads to a divergence of the density of states at the Fermi level.

The use of such resistive thermistors in magnetic field as thermometer (in a bolometer, for instance), gives the user the chance to match the impedance of the thermistor by varying either the magnetic field or the temperature; moreover the magnetic field has the effect to increase the sensitivity of the thermistor to temperature variations, hence enhancing the performance of the bolometer itself.

Chapter 7

Conclusions

During this work of thesis we have focused our attention on the ultra low temperature ($T < 300$ mK) properties of Neutron Transmutation Doped Germanium. NTD Germanium is often used as temperature sensor in low temperature detectors since its resistivity is dependent on temperature. Moreover, its crystalline structure provides a very low heat capacity[30], and hence it is a good candidate to be the temperature sensor of a bolometer.

As a matter of fact, NTD Germanium has been chosen by the CUORE-Cuoricino collaboration to be the thermal sensor of their detector. The KATRIN experiment could get benefits by using a low temperature detector equipped with NTD Ge sensors; since the experiment is in magnetic field, the properties of NTD Ge in magnetic field have been investigated, chapter 6.

NTD germanium is produced (a detailed description is given in §(4.1)) by irradiation of an ultrapure Ge crystal by means of thermal neutrons. Neutrons are captured by some Ge atoms of the lattice and become unstable dacaying into either As, or Ga or Se.
Due to the low neutron capture cross section and to the the Germanium natural isotope composition, the resulting doping is of type p and it is very uniform all over the crystal. The doping density can be changed, relatively easily by increasing the time the Ge crystal is exposed to the neutron flux. Doping density as high as 10^{17} cm^{-3} (around the metal insulator transition)

can be easily reached.

NTD germanium is a semiconductor in which the electrical transport is in a Variable Range Hopping regime with a gap of the density of states of single particle at the Fermi level (§(2.1)) In this regime the electrical resistivity is expressed by the, so called, Mott's Law Equation (2.13):

$$\rho = \rho_p \exp\left(\frac{T_p}{T}\right)^p$$

where the exponent p is directly related to the density of states of single particle at the Fermi level, §(2.1.3).
A general belief is that for NTD Germanium a Coulomb interaction between dopants generates the so called Coulomb Gap §(2.1.3), and hence the latter equation shows $p = 1/2$.
In §(4.2) and §(4.3) we report the experimental results and comparison with the literature. Although data fits reasonably well the Mott law with $p = 1/2$, Figure (4.3), it is evident, Figure (4.5), that letting the p parameter to vary the data are fitted with less deviation. Moreover, the p parameter seems to vary with the doping density. The merge of our data and that of Woodcraft et al. [53], shown in Figure (4.6), covers a relatively large range of doping density, and shows a substantial dependence of p from the doping.

The behaviour of NTD germanium in low temperature and strong magnetic field (60 – 200 mK, and 0 – 5 Tesla) have been investigated in chapter 6. A crossover between a coulomb gap regime in no magnetic field, $p \approx 1/2$ to a regime in which $p \approx 1/3$, in magnetic field has been found (§(6.2.1), Figure (6.4)).
As seen in §(2.3), the $p = 1/3$ is typical of semiconductors in Variable Range Hopping regime, in magnetic field, with no Coulomb Gap. Apparently the effect of the magnetic field is to lower the effectiveness of Coulomb gap. Further increase of magnetic field results in a lowering of the p to values of about 0.15. Such values are not explained by the developed theory, and to our knowledge, no other author report such a value. Different behaviour with respect to the direction of the magnetic field and charge carriers motion was found. Orthogonal samples behave as previously discussed, while the parallel

one shows a sharp decrease of the p parameter to the value of 0.15 with no change within the investigated magnetic field intensities.

Finally, we have investigated the ultra low temperature non linearities of I-V curves (load) curves of the NTDs, and we have tried to fit the experimental data in the frame of the Hot Electron Model, chapter 5. The NTD can be seen as if made out of two subsystems: electrons and phonons. These two system interact; the strenght of the interaction is decreasing with the temperature. As a matter of fact, the possibility of an interaction between a phonon and an electron depends from the number of final states that they can occupy. Since this number is decreasing with temperature, the coupling of the two subsystem is also decreasing.
The interaction between phonons and electrons can be modellized by a thermal conductivity $k_{e\phi}(T)$, Equation (2.26), that links the two subsystems. We have, hence, measured this thermal conductivity for three NTD samples covering the widest range of doping density possible, in order to try to find a possible doping dependence of this parameter. Our three measurements show a conductivity that it is increasing with the doping density, but more measurements must be done.
From literature we see that the measured conductivity are not so easily compared: not all the authors actually fit Equation (2.26), and many authors give different results on the same NTD chip; anyway a comparison of the evaluated $k_{e\phi}(T)$ at 30 mK yelds relatively homogeneus values.

The electron-phonon decoupling is a parameter that plays a fundamental role in determining the pulse shape of a Cuoricino-CUORE bolometer: a large decoupling leads to a pulse height lower than expected. With the measured data, we see that at 20 mK, the electron-phonon decoupling has the same order of magnitude of the boundary thermal resistance, that links the NTD to the heat sink. Anyway, the role of the electron-phonon decoupling, together with that of the boundary resistance can be decreased if the wires, connecting the NTD to the electronics, are thermalized on the absorber instead of to be directly connected to the heat sink.
In the configuration depicted in Figure (7.1), the electrical connections of the NTD are thermally coupled to the absorber and then to the heat sink: the

kapitza boundary resistance, together with the electron-phonon decoupling are in parallel with the thermal conductivity of the electrical connection. A better coupling of the thermistor with the absorber can be gained, and a better resolution can be achieved.

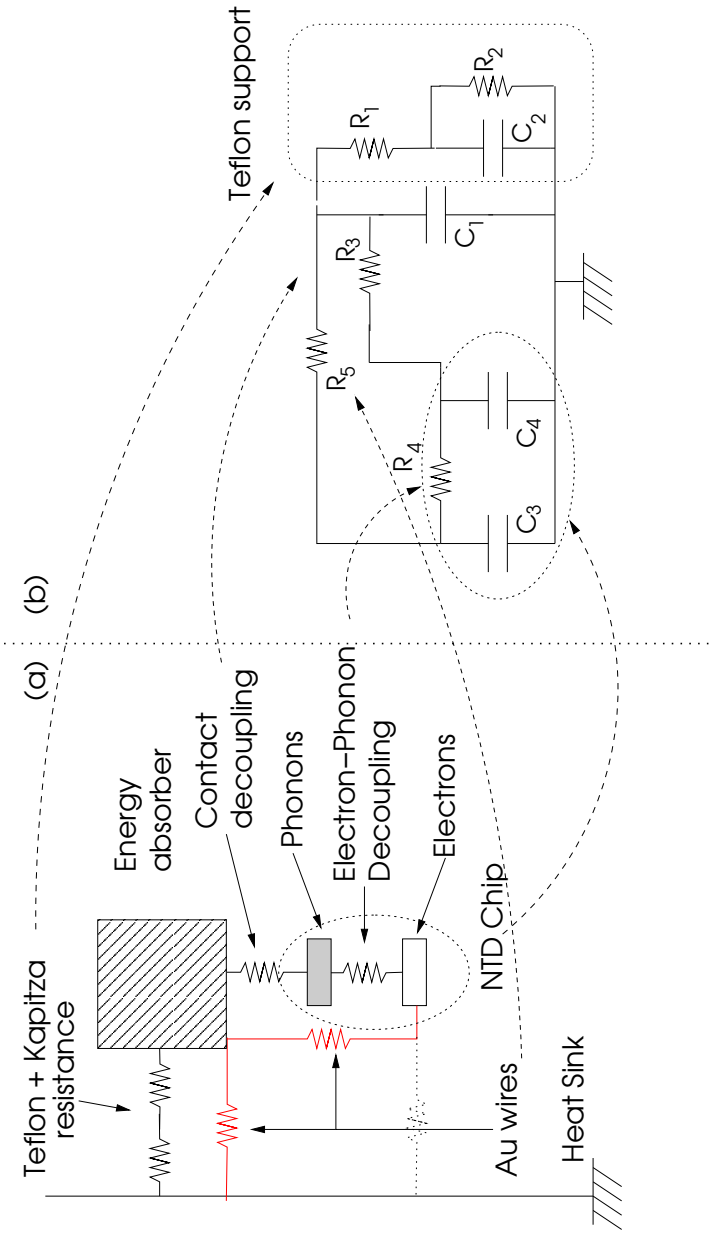

Figure 7.1: If the electrical connections from the NTD thermistor, are thermally coupled to the absorber, R_5 goes in parallel to R_4 and R_3, increasing in this way the coupling of the thermal sensor to the absorber. Note the difference with Figure (1.3) in which R_5 is direclty connected to the heat sink (dotted resistance).

Bibliography

[1] Ahmad Q.R. et al.: *Direct Evidence for Neutrino Flavor Transformation from Neutral-Current Interactions in the Sudbury Neutrino Observatory*
Phys. Rev. Lett. **89**, pag. 11301 (2002)

[2] Fukuda S. et al.: *Constraints on Neutrino Oscillations Using 1258 Days of Super-Kamiokande Solar Neutrino Data*
Phys. Rev. Lett. **86**, pag. 5656 (2001)

[3] Kajita T., Totsuka Y.: *Observation of atmospheric neutrinos*
Rev. Mod. Phys. **73**, pag. 85 (2001)

[4] Eguchi K. et al.: *First Results from KamLAND: Evidence for Reactor Antineutrino Disappearance*
Phys. Rev. Lett. **90**, pag. 21802 (2003)

[5] Feruglio F. et al.: *Neutrino oscillations and signals in β and $0\nu 2\beta$ experiments*
Nucl. Phys. B **637**, pag. 345 (2002)

[6] Pascoli S. et al.: *On the neutrino mass spectrum and neutrinoless double-beta decay*
Phys. Lett. B **558**, pag. 141 (2003)

[7] Joaquim: *Neutrino masses from beta decays after KamLAND and WMAP*
Phys. Rev. D **68**, pag. 33019 (2003)

[8] Elgarøy O. et al.: *New Upper Limit on the Total Neutrino Mass from the 2 Degree Field Galaxy Redshift Survey*
Phys. Rev. Lett. **89**, pag. 61301 (2002)

[9] Lobashov V. M.: *The search for the neutrino mass by direct method in the tritium beta-decay and perspectives of study it in the project KATRIN*
Nucl. Phys. A **719**, pag. 153 (2003)

[10] Elliot S. et al.: Annu. Rev. Nucl. Part. Sci. **52**, pag. 115 (2002)

[11] Cremonesi O.: Nucl. Phys. B (Proc. Suppl.) **118**, pag. 287 (2002)

[12] Ejiri H.: Prog. Part. Nucl. Phys. B **48**, pag. 185 (2002)

[13] Klapdor-Kleingrothaus H.V. et al.: Mod. Phys. Lett. A **16**, pag. 2409 (2002)

[14] Harney L. et al.: Mod. Phys. Lett. A **16**, pag. 2409 (2001)

[15] Aalseth C.E. et al.: Mod. Phys. A **17**, pag. 1475 (2002)

[16] Zdesenko Yu.G. et al.: Phys. Lett. B **546**, pag. 206 (2002)

[17] Bakaliarov A.M. et al.: *Results of the experiment on investigation of Germanium 76 Double Beta Decay*
Proc of NANP2003 (2003)

[18] Turkevich A.L. et al.: Phys. Rev. Lett. **67**, pag. 3211 (1992)

[19] Lee J.T. et al.: Nucl. Phys. A **529**, pag. 221 (1991)

[20] Bernatowicz T. et al.: Phys. Rev. Lett. **69**, pag. 2341 (1992)

[21] Takaoka N. et al.: Phys. Rev. C **53**, pag. 1557 (1993)

[22] Kawashima A. et al.: Phys. Rev. C **47**, pag. 2452 (1993)

[23] Dell'Antonio G.F. et al.: Suppl. Nuovo Cimento **17**, pag. 132 (1960)

[24] Fiorini E. et al.: Nucl. Instrum. Meth. **224**, pag. 83 (1984)

[25] Booth N. et al.: Annu. Rev. Nucl. Part. Sci. **46**, pag. 471 (1996)

[26] Scott Porter F. et al.: Proc. LTD 2001 Madison WI **605**, pag. 0 (2001)

[27] Dyck G.R. et al.: Phys. Lett. B **245**, pag. 343 (1990)

[28] Arnaboldi C. et al.: Phys. Lett. B **557**, pag. 167 (2003)

[29] Bettini A.: Phys. Usp. **170**, pag. 977 (2001)

[30] Pedretti M et al.: *Measurement of thermal properties for modeling and optimization of large mass bolometers*
Physica B **329**, pag. 1614 (2003)

[31] Frank Pobell: *Matter and Methods at Low Temperatures*
Springer-Verlag (1992)

[32] Anderson P.W.: *Absence of Diffusion in Certain Random Lattices*
Phys. Lett. **109**, pag. 1492 (1958)

[33] Shkolvskii B.I. Efros A.L.: *Electronic Properties of Doped Semiconductors*
Springer-Verlag (1984)

[34] Srinivasan G.: *Statistical Mechanics of Charged Traps in an Amorphous Semiconductor*
Phys. Rev. B **4**, pag. 2851 (1971), and reference therein

[35] Wang N. et al.: *Electrical and Thermal properties of neutron-transmutation-doped Ge at 20 mK*
Phys. Rev. B **41**, pag. 3761 (1990)

[36] Zhang J. et al.: *Non-Ohmic effects in hopping conduction in doped silicon and germanium between 0.05 and 1 K*
Phys. Rev. B **57**, pag. 4472 (1998)

[37] Soudee J. et al.: *Hot Electron Effect in a #23 NTD Ge Sample*
J. Low Temp. Phys. **110**, pag. 1013 (1998)

[38] Watanabe M. et al.: *Electrical properties of isotopically enriched neutron-transmutation-doped ^{70}Ge:Ga near the metal-insulator transition*
Phys. Rev. B **58**, pag. 9851 (1998)

[39] Pasca E. et al.: *Measurement of Electron-Phonon Decoupling in NTD31 Germanium*
World Scientific Proc. ICATPP 7th, pag. 684 (2002)

[40] Miller, A., Abrahams E.: *Impurity Conduction at Low Concentrations*
Phys. Rev. **120**, pag. 745 (1960)

[41] Pollak M., Reiss J.: J. Phys. C **9**, pag. 2339 (1976)

[42] Little W.A.: Can. J. Phys. **37**, pag. 334 (1959)

[43] Anderson A.C, Peterson R.E.: *Thermal Resistance between Electrons and Phonons in Copper*
Phys. Lett. **38**, pag. 519 (1972)

[44] Raikh M. E. et al.: *Mechanism of magnetoresistance in variable-range-hopping transport for two-dimensional electron systems*
Phys. Rev. B **45**, pag. 6015 (1992)

[45] De Moor P. et al.: *Calorimetric single particle detection in high magnetig fields at low temperatures*
J. Appl. Phys. **79**, pag. 3811 (1996)

[46] Shlimak I. S. et al.: *Density of states near the Fermi level from measurements of variable-range-hopping magnetoresistance in germanium*
Phys. Rev. B **48**, pag. 11796 (1993)

[47] Shlimak I. et al.: *Crossover Phenomenon for hopping conduction in strong magnetic fields*
Phys. Rev. Lett. **68**, pag. 3076 (1992)

[48] Sladek R.L.: *Magnetically induced impurity banding*
J. Phys. Chem. Solids **5**, pag. 157 (1958)

[49] Pedretti M. et al.: *Insubria-Florence development of a 10 millikelvin reactive bolometer for the detection of rare events*
World Scientific Proc. ICATPP 8th, pag. 196 (2003)

[50] Wang N.: *A Cryogenic Phonon Detector to Search for Dark Matter Particles*
Dissertation UC Berkeley (1984)

[51] Haller E.E.: *Advanced Far-Infrared Detectors*
Infrared Phys. Technol. **35**, pag. 127 (1994)

[52] Pasca E. et al.: *Low Temperature Properties of NTD Germanium: best Choice for CUORE*
World Scientific Proc. ICATPP 8th, pag. 93 (2003)

[53] Woodcraft A.L. et al.: *Hopping Conduction in NTD Germanium: Comparison between Measurement and Theory*
J. Low Temp. Phys. **134**, pag. 925 (2004)

[54] Aubourg E. et al.: J. Low Temp. Phys. **93**, pag. 289 (1993)

[55] Alessandrello A. et al.: Workshop on Semiconductor thermistor for mK operation, UC Berkeley (1991)

[56] Uhlig K.: Cryogenics **35**, pag. 525 (1995)

*

Appendix A

Publication List

1. Monticone E et al.: *Characterization of Titanium Films for low temperature detectors*
   Proc. LTD-9 Madison (WI), pag. 181 (2001)

2. Pasca E. et al.: *Measurement of Electron-Phonon Decoupling in NTD31 Germanium*
   World Scientific Proc. ICATPP 7th **605**, pag. 684 (2002)

3. Ventura G. et al.: *Low temperature Thermal Properties of PolyPropylene*
   Cryogenics **42**, pag. 551 (2002)

4. Barucci M. et al.: *Low Temperature Thermal Properties of support material for massive cryogenic detectors*
   World Scientific Proc. ICATPP 7th **605**, pag. 668 (2002)

5. Ventura G et al.: *Development of Ti based Transition Edge Sensors for Cryogenic detectors*
   World Scientific Proc. ICATPP 7th **605**, pag. 677 (2002)

6. Olivieri E. et al.: *Thermal expansion coefficient of cold-pressed Silicon Carbide*
   World Scientific Proc. ICATPP 8th, pag. 593 (2003)

7. Barucci M. et al.: *Aluminium alloys for space applications: low temperature thermal conductivity of A6061-T6 and A1050*
   World Scientific Proc. ICATPP 8th, pag. 541 (2003)

8. Pasca E. et al.: *Low Temperature Properties of NTD Germanium: best Choice for CUORE*
   World Scientific Proc. ICATPP 8th, pag. 93 (2003)

9. Risegari L. et al.: *Very-low-temperature thermal conductivity of polymeric supports for massive cryogenic detectors*
   World Scientific Proc. ICATPP 8th, pag. 603 (2003)

10. Giuliani A et al.: *CUORE: low-temperature techniques for neutrino physics*
    Physica B **329**, pag. 1570 (2003)

11. Gandini C. et al.: *Correlation of Critical Temperatures and Electrical Properties in Titanium Films*
    Int. J. Modern Phys. B **17**, pag. 948 (2003)

12. Pedretti M et al.: *Measurement of thermal properties for modeling and optimization of large mass bolometers*
    Physica B **329**, pag. 1614 (2003)

13. Pedretti M. et al.: *Insubria-Florence development of a 10 millikelvin reactive bolometer for the detection of rare events*
    World Scientific Proc. ICATPP 8th, pag. 196 (2003)

14. Pasca E. et al.: *Thermal conductivity of Torlon between 4.2 and 300 K*
    Proc. TEMPMEKO 2004 (2004)

15. Cinti F. et al.: *Chiral Phase Transition on quasi-1D Molecular Magnet Gd(hfac)3NlTiPr*
    Proc. ICMM 2004 Tsukuba (2004)

16. Risegari L. et al.: *Measurement of the thermal conductance of copper samples between 30 and 150 mK*
    Cryogenics **44**, pag. 875 (2004)

17. Bucci C. et al.: *First results from the Cuoricino experiment*
    Nucl. Instr. Meth. A **520**, pag. 132 (2004)

18. Arnaboldi C et al.: *First results on neutrinoless double beta decay of Te-130 with the calorimetric CUORICINO experiment*
    Phys. Lett. B **584**, pag. 260 (2004)

19. Risegari L. et al.: *Use of good copper for the optimization of the cooling down procedure of large masses*
    Cryogenics **44**, pag. 167 (2004)

20. Pasca E. et al.: *Very-Low-Temperature capacitance sensors*
    Proc. TEMPMEKO 2004 (2004)

21. Barucci M. et al.: *Thermal conductivity of Torlon between 4.2 and 300 K*
    Cryogenics accepted proof in print (2004)